Supporting information for "The Important Contribution of Secondary Formation and Biomass Burning to Oxidized Organic Nitrogen (OON) in a Polluted Urban Area: Insights from In Situ FIGAERO-CIMS Measurements"

Yiyu Cai[1,2,3,4,5*], Chenshuo Ye[6*], Wei Chen[1,2,3,4,5], Weiwei Hu[1,2,3,4], Wei Song[1,2,3,4], Yuwen Peng[7,8], Shan Huang[7,8], Jipeng Qi[7,8], Sihang Wang[7,8], Chaomin Wang[7,8], Caihong Wu[7,8], Zelong Wang[7,8], Baolin Wang[9], Xiaofeng Huang[10], Lingyan He[10], Sasho Gligorovski[1,2,3,4], Bin Yuan[7,8], Min Shao[7,8], Xinming Wang[1,2,3,4]

[1]State Key Laboratory of Organic Geochemistry, Guangzhou Institute of Geochemistry, Chinese Academy of Sciences, Guangzhou 510640. China
[2]CAS Center for Excellence in Deep Earth Science, Guangzhou, 510640, China
[3]Guangdong-Hong Kong-Macao, Joint Laboratory for Environmental Pollution and Control, Guangzhou Institute of Geochemistry, Chinese Academy of Science, Guangzhou 510640, China
[4]Guangdong Provincial Key Laboratory of Environmental Protection and Resources Utilization, Chinese Academy of Science, Guangzhou 510640, China
[5]University of Chinese Academy of Sciences, Beijing 100049, China
[6]Guangdong Provincial Academy of Environmental Science, Guangzhou, 510640, China
[7]Institute for Environmental and Climate Research, Jinan University, Guangzhou 511443, China
[8]Guangdong-Hongkong-Macau Joint Laboratory of Collaborative Innovation for Environmental Quality, Guangzhou 511443, China
[9]School of Environmental Science and Engineering, Qilu University of Technology, Jinan 250353, China
[10]Key Laboratory for Urban Habitat Environmental Science and Technology, School of Environment and Energy, Peking University Shenzhen Graduate School, Shenzhen, 518055, China

*Yiyu Cai and Chenshuo Ye contributed equally to this work.
Correspondence to: Weiwei Hu (weiweihu@gig.ac.cn); Bin Yuan (byuan@jnu.edu.cn).

Contents of this file

Text S1: Intercomparison of AMS-derived organic nitrates based on multiple methods

Nitrate signals (NO^+, NO_2^+, HNO_3^+) measured by a high-resolution time-of-flight aerosol mass spectrometer (HR-ToF-AMS) include both organic nitrates and inorganic nitrates. Many methods were established to separate the total measured nitrates from inorganic nitrates and particle-phase organic nitrates (i.e., the particle-phase nitrate functional group, $pOrgNO_{3,\ AMS}$), i.e., NO_2^+/NO^+ ratio method (Farmer et al., 2010), Positive Matrix Factorization (PMF) method (Hao et al., 2014; Sun et al., 2012; Xu et al., 2015) and Thermodenuder (TD) method (Xu et al., 2021). In this study, these three methods were applied to quantify $pOrgNO_{3,\ AMS}$. Note that in agreement with Dancey and Reidy (2007), we interpreted the absolute value of the Pearson correlation coefficient as (i) no correlation, if $|r| \leq 0.1$; (ii) weak correlation, if $0.1 < |r| \leq 0.3$; (iii) moderate correlation, if $|0.3 < r| \leq 0.7$; (iv) strong correlation, if $0.7 < |r| \leq 1$; and finally, (v) perfect correlation, if $|r| = 1$.

(1) **NO_2^+/NO^+ ratio method.** Previous studies have reported much lower NO_2^+/NO^+ ratios of $pOrgNO_{3,\ AMS}$ (R_{ON}) than that of inorganic nitrates, i.e., NH_4NO_3 ($R_{NH_4NO_3}$) (Boyd et al., 2015; Farmer et al., 2010; Fry et al., 2013; Sato et al., 2010). Fry et al. (2013) quantified that the R_{ON} ratio is 2.25 times lower than the $R_{NH_4NO_3}$ based on multiple results using different AMSs in chamber studies. Recently, Day et al. (2022) and Fry et al. (2018) summarized more studies and redefined the ratio $R_{NH_4NO_3}/R_{ON}$ to be 2.75. The average $R_{NH_4NO_3}$ was estimated to be 0.37 from the standard calibration of NH_4NO_3, which is quite stable across this entire campaign. Then, the R_{ON} for this study was estimated to be 0.13 based on the $R_{NH_4NO_3}/R_{ON}$ ratio of 2.75.

Thus, the fraction of $pOrgNO_{3,\ AMS}$ in total nitrates (ON_{frac}) measured by the AMS can be calculated as (Farmer et al., 2010):

$$ON_{frac} = \frac{\left(R_{ambient}\text{-}R_{NH_4NO_3}\right)(1+R_{ON})}{\left(R_{ON}\text{-}R_{NH_4NO_3}\right)(1+R_{ambient})} \quad \text{(S1)}$$

where $R_{ambient}$ is the NO_2^+/NO^+ ratio of ambient nitrate. The final concentration of $pOrgNO_{3,\ AMS}$ can be calculated based on total nitrates and ON_{frac} . To calculate the uncertainty of ON_{frac} with the NO_2^+/NO^+ ratio method, ratios of 2.08 and 4.17 (R_{ON} = 0.18 and 0.09) obtained from isoprene- and monoterpene-derived $pOrgNO_{3,\ AMS}$, were used for calculating the upper (mean 0.85 μg m^{-3}) and lower (mean 0.53 μg m^{-3}) bounds of $pOrgNO_{3,\ AMS}$ (Xu et al., 2015; Xu et al., 2021), respectively. When the ambient nitrate signal is high in ambient air (e.g., >5 ug m^{-3}), the high nitrate signal was mainly contributed by the inorganic ammonium nitrate (Day et al., 2022). This leads to that the NO_2^+/NO^+ ratio of ambient nitrate is similar to that of pure inorganic ammonium nitrate, thus resulting in a large uncertainty in $pOrgNO_{3,\ AMS}$ estimation. This issue had been fully addressed in the method paper on how to estimate $pOrgNO_{3,\ AMS}$ from AMS measurement (Day et al., 2022). The larger uncertainty of estimated $pOrgNO_{3,\ AMS}$ by AMS under high nitrate signal periods has also been found in other ambient studies (Yu et al., 2019; Zhu et al., 2016).

(2) **PMF method**. It is well known that the PMF analysis can be used for source appointment and estimation of various organic factors, e.g., primary organic aerosol and secondary organic aerosol (SOA). Combining the OA spectral matrix with NO^+ and NO_2^+ ions detected by AMS, different OA factors including organic NO^+ and NO_2^+ ions can provide insights regarding the relative contributions of $pOrgNO_{3,\ AMS}$ and inorganic nitrates (Sun et al., 2012; Xu et al., 2015). Therefore, the concentrations of $pOrgNO_{3,\ AMS}$ (NO^+_{org} and $NO^+_{2,org}$) are equal to the sum of NO^+ and NO_2^+ via Eqs. (S2) and (S3) (Xu et al., 2015):

$$NO^+_{2,org} = \sum \left([\text{OA factor}]_i \times f_{NO_2,i} \right) \quad \text{(S2)}$$

$$NO^+_{org} = \sum \left([\text{OA factor}]_i \times f_{NO,i} \right) \quad \text{(S3)}$$

where $[\text{OA factor}]_i$ is the mass concentration of OA factor i, $f_{NO_2,i}$ and $f_{NO,i}$ are the mass fractions of NO_2^+ and NO^+ in each factor, respectively.

(3) **TD method.** The method was developed for the estimation of $pOrgNO_{3,\ AMS}$ from the measurement of HR-ToF-AMS coupled with a thermodenuder based on the difference of volatility between $pOrgNO_{3,\ AMS}$ ($NO^+_{x,org}$) and inorganic nitrates ($NO^+_{x,inorg}$) in particles (Xu et al., 2021). It is assumed that (I) the remaining mass loading of nitrate fragments was dominated by $NO^+_{x,org}$, while $NO^+_{x,inorg}$ evaporated completely at T = 90℃ due to the higher volatility of $NO^+_{x,inorg}$ than $NO^+_{x,org}$ (Huffman et al., 2008; Ng et al., 2017); (II) The $C_xH_yN^+_z$ and $C_xH_yO_zN^+_p$ ions were supposed to have similar volatility as $NO^+_{x,org}$ which dominate the remaining fragments at T > 90℃ (Xu et al., 2021). Combined with the two assumptions, the mass concentration of $pOrgNO_{3,\ AMS}$ ($[NO_{3,org}]$) in the ambient atmosphere can be determined by Eq. (S4) (Xu et al., 2021):

$$[NO_{3,org}] = \frac{[NO_3]_{T=90℃}}{MFR_{CHN^+ + CHON^+ T=90℃}} \quad \text{(S4)}$$

The subscript "T = 90℃" denotes the mass concentration or the mass fraction remaining (MFR) of fragments at T = 90℃.

The intercomparison of $pOrgNO_{3,\ AMS}$ based on these three methods and the particle-phase oxidized organic nitrogen (pOON) measured by an iodide chemical ionization time-of-flight mass spectrometer installed with a Filter Inlet for Gases and AEROsols (FIGAERO-CIMS) in this campaign are presented in Fig. S2. The average concentrations of $pOrgNO_{3,\ AMS}$ and pOON are shown in Table S2. Generally, the $pOrgNO_{3,\ AMS}$ derived from PMF method increases with total nitrates and is largely overestimated compared to other methods during the high nitrate periods. The $pOrgNO_{3,\ AMS}$ estimated from the TD method correlates well (R = 0.73) with that from NO_2^+/NO^+ ratio method. However, the former exhibits noisier especially under low nitrate periods probably

due to the large uncertainty of the lower mass remaining fraction for $pOrgNO_{3,\ AMS}$ at higher temperature (>90°C). T = 90°C was assumed to represent the temperature mentioned above at which inorganic nitrates have been evaporated completely. However, this might not be the case in some environments (Huffman et al., 2008). The drawback of NO_2^+/NO^+ ratio method is the slightly large uncertainty under high NO_x conditions such as during 25−26 October 2018 (Fig. S2a).

Finally, we chose NO_2^+/NO^+ ratio method for more analysis in the main text given its smooth profile and relative stable estimation of total $pOrgNO_{3,\ AMS}$ (Yu et al., 2019). The average mass fraction of $pOrgNO_{3,\ AMS}$ to total nitrates is 15% and that mass fraction increases with decreasing concentration of total nitrates (Fig. S2b), indicating the dominant role of pON chemistry under low nitrate atmospheric environment.

Text S2: The calculation of the production rate of gas-phase organic nitrates

In the presence of NO, the production rate of gas-phase oxidized organic nitrogen (gOON) from hydroxyl radical (OH) initiated oxidation with volatile organic compounds (VOCs) (P_{ON}^{OH}) can be calculated following Eq. (S5) (Liebmann et al., 2019):

$$P_{ON}^{OH} = [OH]\beta \sum \alpha_i^{RO_2} k_i^{OH} [C_i] \quad \text{(S5)}$$

where [OH] is the concentration of OH, which was obtained from a box model simulation based on master chemical mechanism v3.3.1 (MCM v3.3.1) (Wang et al., 2020; Wolfe et al., 2016). $[C_i]$ is the concentration of speciated VOC *i*. k_i^{OH} is the reaction rate coefficient between OH and VOC *i*, $\alpha_i^{RO_2}$ is the formation branching ratio of gOON for speciated VOC *i*, β represents the fraction of the peroxy radicals (RO_2) that react with NO which can be estimated by $\beta = \frac{k_{RO_2+NO}[NO]}{k_{RO_2+NO}[NO]+k_{RO_2+HO_2}[HO_2]}$ ($k_{RO_2+NO} = 9.0 \times 10^{-12}$ and $k_{RO_2+HO_2} = 2.3 \times 10^{-11}$ cm^3 $molecule^{-1}$ s^{-1} from MCM v3.3.1) (http://mcm.leeds.ac.uk/MCMv3.3.1/home.htt). The estimated values of β were 0.98−1.0 during the campaign, thus $\beta = 1$ was used in this calculation. The VOC species, reaction rate coefficients, yields, and branching ratios used for this calculation can be found in Table 1.

The nitrate radical (NO_3) concentration was calculated based on measured N_2O_5 by the CIMS assuming temperature equilibrium between these two species (Brown and Stutz, 2012). Then the gOON production rate from NO_3 initiated oxidation of VOC ($P_{ON}^{NO_3}$) can be calculated by Eq. (S6):

$$P_{ON}^{NO_3} = \sum \alpha_i k_{NO_3+C_i} [C_i][NO_3] \quad \text{(S6)}$$

where $[C_i]$ and $[NO_3]$ are the concentrations of speciated VOC *i* and NO_3, α_i is the gOON yield, $k_{NO_3+[C_i]}$ is the reaction rate coefficient as shown in Table 1. The reactions between alkanes and NO_3 are very slow accounting for negligible chemical changes

in the ambient atmosphere so that alkanes were not included in this calculation. The VOC species of terpenes, aromatics, and alkenes (Table 1) measured during October 2018 were used to calculate the NO_3 loss rate. Only 2% of the NO_3 loss rate was attributed to alkenes. And the NO_3 loss rate attributed to cresol and phenol (30% on average, ranging from 13% to 60%) was three orders of magnitude higher than the other aromatics (~0.1%). Thus, we assumed that the alkanes, alkenes, and the other aromatics (excluding cresol and phenol) contributed little (<3%) to the total gOON production rate, which were not included in this calculation.

The gOON production rate of ozone (O_3) initiated oxidation of VOC ($P_{ON}^{O_3}$) can be calculated by Eq. (S7):

$$P_{ON}^{O_3} = [O_3]\beta \sum \alpha_i^{O_3} k_i^{O_3} [C_i] \alpha_i^{RO_2} \quad \text{(S7)}$$

where $[O_3]$ is the concentration of O_3, $k_i^{O_3}$ is the reaction rate coefficient between O_3 and VOC i, $\alpha_i^{O_3}$ is the yield of RO_2, and $\alpha_i^{RO_2}$ is the ON yield of the reaction RO_2+NO for speciated VOC (Table 1). β and $[C_i]$ are the same as in Eq. (S5). The short-chain alkenes including propene, butene and pentene yield negligible SOA as well as ON, thus we did not include them in the calculation.

Fig. S3 shows the time series and average diurnal variations of OH, NO_3, and O_3 used in the calculation above. The average concentration of OH was $1.11 \pm 1.86\times10^6$ molecule m^{-3} which peaks at noon (mean $4.20 \pm 2.69\times10^6$ molecule m^{-3}). The averaged mixing ratio of NO_3 was 1.14 ± 2.82 ppt which peaks at 18:00 (2.25 ± 3.85 ppt) and night (2.35 ± 5.00 ppt), consistent with other studies in urban areas (Hamilton et al., 2021; Wang et al., 2017). No speciated monoterpene measurement was conducted in this campaign. Thus, we assume that the monoterpenes at this urban site were contributed by limonene and α-pinene with a ratio of 1:1 during this campaign. A recent study found that half of the ambient monoterpenes can be attributed to the VCP-dominated source based on measurements at altitude of 450 m in the Canton Tower in Guangzhou urban area (Li et al., 2022). The other half monoterpenes are mainly from visitor-related emissions since Canton tower is a tourism site. It is consistent with our finding that the ambient monoterpenes in this study is anthropogenic origins. Gkatzelis et al. (2021) found the limonene was the dominant isomer of monoterpenes in VCP emissions. And *Coggon et al.* (2021) found the α-pinene (19%) and limonene (53%) were the main isomers of monoterpene in the center of megacity New York. Thus, a 1:1 assumption of limonene and α-pinene applied here shall be reasonable. The concentration of sesquiterpenes could be calculated as a function of the monoterpene concentration, as described in Sommers et al. (2022). Since a large fraction of monoterpene in this study was assumed to be anthropogenic, thus, the calculated concentration of sesquiterpenes herein is a high limit. The calculated mass concentration of the sesquiterpenes is only 7% of the monoterpene concentration in this campaign. Omitting the sesquiterpenes in the gOON production rate calculation should be within the estimated uncertainty of the gOON production rate. In addition, the yield parameters for gOON production

rate from sesquiterpenes were missed. Thus, in this study, sesquiterpenes were not accounted for in the final gOON production rate calculation.

Text S3: Uncertainty of gOON production rate estimation.

Monte Carlo method was used to estimate the entire uncertainty of the gOON production rate with 10,000 calculations as shown in Fig. S4. During the Monte Carlo method, the kinetic parameter sets were assigned according to Liebmann et al. (2019), which can involve the uncertainties of varies parameters, e.g., yields and branch ratios. Then the parameters were allowed randomly vary within the range and vast number of combinations of input parameters were used to be computed (Mckay et al., 2000). During the iteration, we estimated the uncertainty in the term NO_3 pathway of 58%, with 50% from [NO_3], 15% from $k_{NO_3+C_i}$, 50% from α_i, and 30% from [C_i]. If 30−50% uncertainties were added to the concentration ratio of α-pinene to limonene, the uncertainty of the term NO_3 pathway increased up to 62−70%. The uncertainty in the term OH pathway was 45%, with 50% from [OH], 15% from k_i^{OH}, 50% from $\alpha_i^{RO_2}$, 30% from β, and 35% from [C_i]. The uncertainty in the term O_3 pathway was 66%, with contribution of 10% from [O_3], 35% from [C_i], 15% from $k_i^{O_3}$, 50% from $\alpha_i^{RO_2}$, 30% from β, and 50% from $\alpha_i^{O_3}$. An overall uncertainty of 56% was estimated by this method.

Text S4: The calculation of aromaticity index and seasonal decomposition

The aromaticity index (AI) is defined for the identification of aromatic and condensed aromatic structures, which was calculated by the Eq. (S8) (Koch and Dittmar, 2016, 2006):

$$AI = \frac{1+c-0.5o-0.5n-0.5h}{c-0.5o-n} \quad \text{(S8)}$$

where c, o, n, and h correspond to the number of C, O, N, and H atoms, respectively, in each molecule.

A time series usually comprises three components: a trend-cycle component, a seasonal component, and a remainder component (containing anything else in the time series). If an additive decomposition was assumed, the Eq. is:

$$y_t = S_t + T_t + R_t \quad \text{(S9)}$$

where y_t is the data, S_t is the seasonal component, T_t is the trend-cycle component, and R_t is the remainder component, all at period t. Taking 24 hours as the "season" in the calculation, we can get a clearer diurnal variation preventing the trend blurred by the varies intensity between days. The detailed process of the calculation applied in this paper can refer to Hilas et al. (2006).

Table S1. The regression slopes between measured gOON (pOON) vs particle-phase levoglucosan in selected biomass burning emission episodes. The average values based on different biomass burning episodes are also shown.

Episode	Slope ($\mu g\ m^{-3}/\mu g\ m^{-3}$)	Episode	Slope ($\mu g\ m^{-3}/\mu g\ m^{-3}$)
Gas phase			
(06)	5.30 ± 2.10	(28)	3.57 ± 0.72
(20)	1.00 ± 0.18 [a]	(30)	3.99 ± 0.87
(22)	4.10 ± 1.54	Average	3.95 ± 1.67
(24)	5.75 ± 1.28		
Particle phase			
(06)	6.66 ± 2.28	(25)	5.14 ± 1.76
(07)	3.14 ± 1.05	(28)	5.61 ± 0.69
(13)	5.23 ± 0.26	(30)	4.37 ± 0.42
(20)	5.11 ± 0.40	Average	5.05 ± 1.01
(22)	5.15 ± 0.88		

Note. [a] The relatively low value from the episode at night on 20 October was also selected for the criteria used here, indicating the special low contribution from biomass burning to gOON during this episode.

Table S2. Summary of average mass concentrations of OON measured or calculated by the CIMS and the AMS, averaged values of gOON production rates, meteorological parameters, and other OON-related parameters during October 2018.

	Average ± SD		Average ± SD
$pOrgNO_{3,\ AMS}$ (μg m^{-3})	--	secondary gOON (μg m^{-3})	0.79 ± 0.67
NO_2^+/NO^+ ratio method	0.60 ± 0.46	**Total gOON production rate (ppb h^{-1})**	0.11 ± 0.11
TD method	1.10 ± 0.81	*OH initiated*	0.07 ± 0.10
PMF method	2.29 ± 2.38	*NO_3 initiated*	0.05 ± 0.07
$pOON_{CIMS}$ (μg m^{-3})	0.66 ± 0.53	*O_3 initiated*	0.01 ± 0.01
$gOON_{CIMS}$ (μg m^{-3})	1.00 ± 0.67	OA (μg m^{-3})	14.27 ± 8.20
$pC_{4-5}N$ (μg m^{-3})	0.10 ± 0.07	Nitrate (μg m^{-3})	4.44 ± 6.05
$pC_{6-9\_aro}N$ (μg m^{-3})	0.10 ± 0.09	$pOON_{CIMS}$/OA	0.05 ± 0.02
$pC_{8-10}N$ (μg m^{-3})	0.27 ± 0.21	NO (ppb)	9.24 ± 18.33
$pC_{11-20}N$ (μg m^{-3})	0.09 ± 0.08	NO_2 (ppb)	31.17 ± 18.38
$pC_{other}N$ (μg m^{-3})	0.12 ± 0.09	O_3 (ppb)	36.95 ± 31.21
levoglucosan (μg m^{-3})	0.06 ± 0.07	wind speed (m s^{-1})	4.50 ± 2.18
BB pOON (μg m^{-3})	0.32 ± 0.36	temperature (°C)	23.73 ± 2.92
secondary pOON (μg m^{-3})	0.34 ± 0.35	RH (%)	71.92 ± 17.43
BB gOON (μg m^{-3})	0.25 ± 0.29		

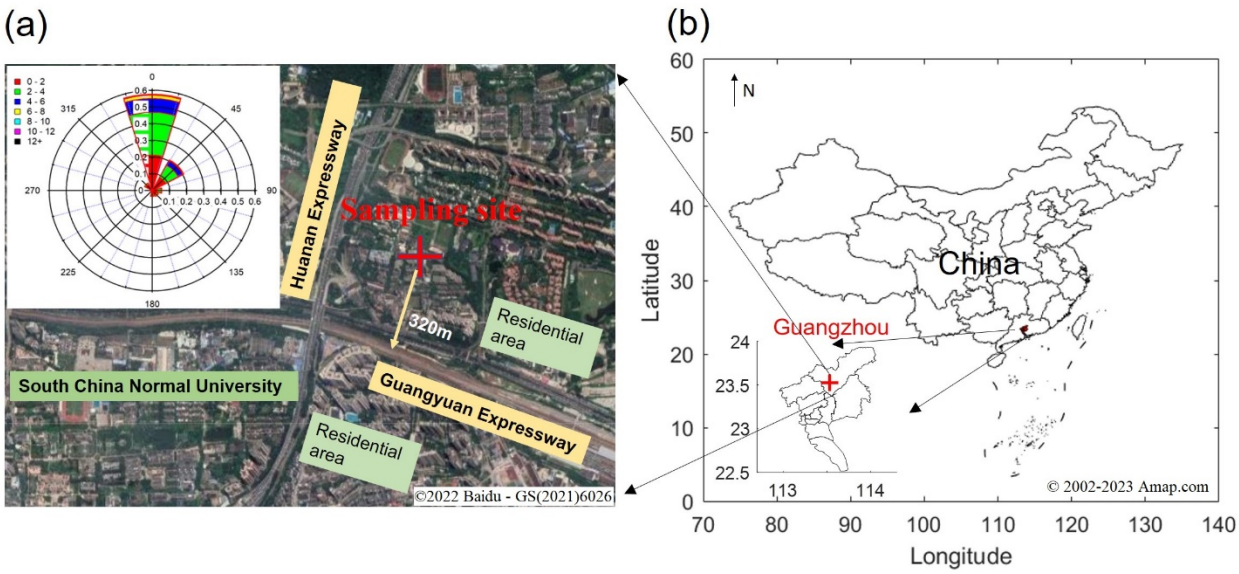

Figure S1. Site descriptions: (a) The satellite view of sampling site in Guangzhou, China. The sampling site is located in the campus of Guangzhou institute of Geochemistry (GIG), Chinese Academy of Sciences (Source: from Baidu Maps, https://map.baidu.com/@12620203.579365265,2633189.008055671,16.34z/m aptype%3DB_EARTH_MAP). The wind rose plot during the campaign is also shown as insert plot with color represents the wind speed. (b) The location of Guangzhou city in the map of China. (Source: from DataV.GeoAtlas. http://datav.aliyun.com/portal/school/atlas/area_selector).

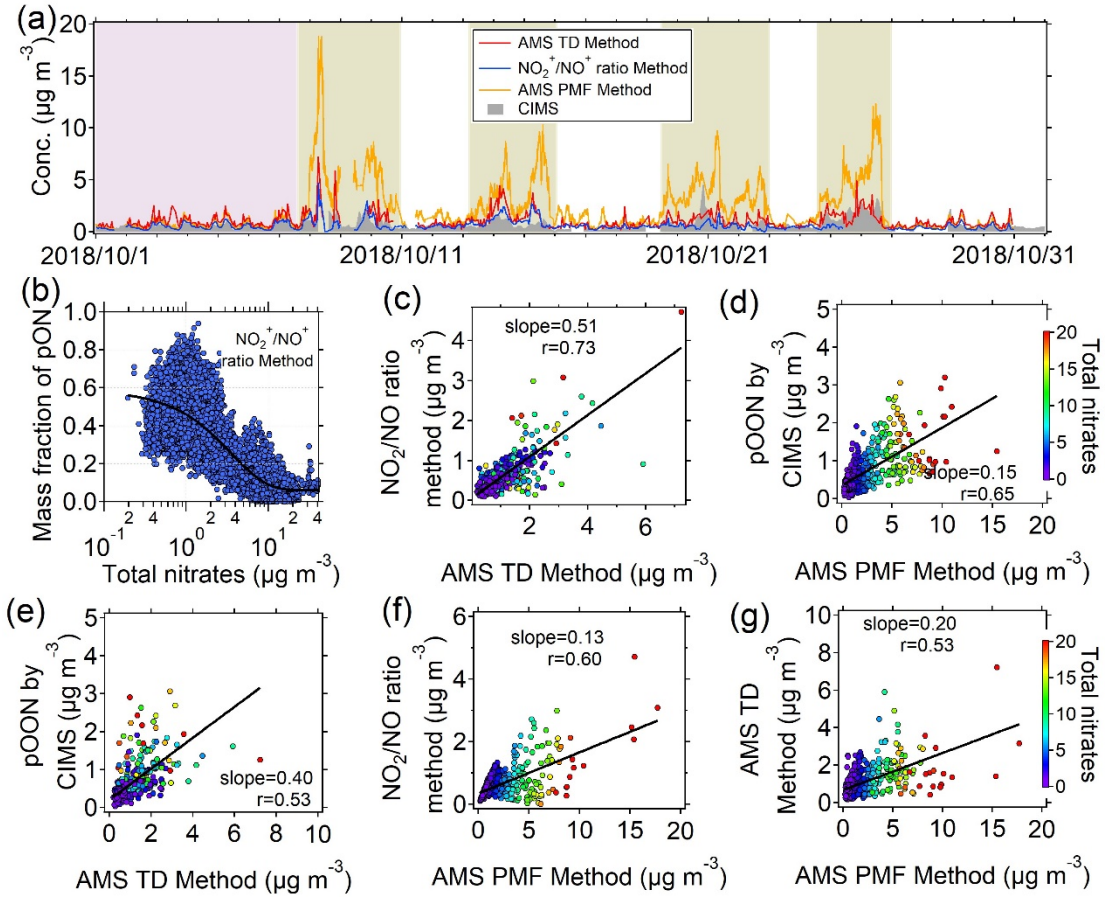

Figure S2. (a) Comparison of time series of pOON derived from the CIMS and $pOrgNO_{3,AMS}$ from the AMS based on three methods introduced in Text S1. The tinted backgrounds with light pink and light yellow indicate the period with low and high concentrations of nitrates, respectively. (b) Mass fraction of $pOrgNO_{3,AMS}$ (NO_2^+/NO^+ ratio method) to total nitrates as a function of total nitrate signal derived from the AMS. (c–g) Scatterplots of pOON measured by the CIMS and $pOrgNO_{3,AMS}$ calculated by three methods based on the AMS measurement. All the scatters are color-coded by the mass concentration of total nitrate signals measured by the AMS. All the linear fitting are based on the orthogonal distance regression (ODR) algorithm in this study.

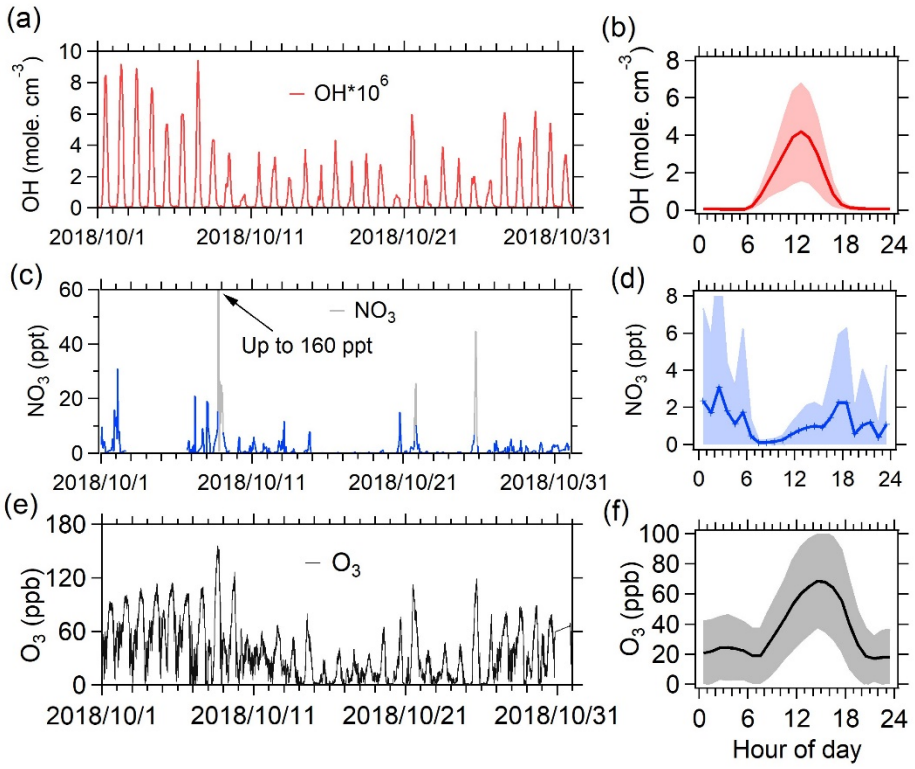

Figure S3. The time series and average diurnal variations of (a, b) OH, (c, d) NO_3 and (e, f) O_3 used in the calculation of the gOON production rate. The shaded areas mean the standard deviations. Based on the on-line measurement of N2O5 by the CIMS, extremely high concentration of NO3 was estimated, which cannot be explained by the box model. To avoid the interferences from extremely high concentration of NO3, the unexplained peaks color-coded using grey in (c) was not included in the final ON calculation. When such high episodes of measured NO3 were included in the calculation of gOON production rate, the contribution of gOON production rate from daytime NO3 oxidation is even larger.

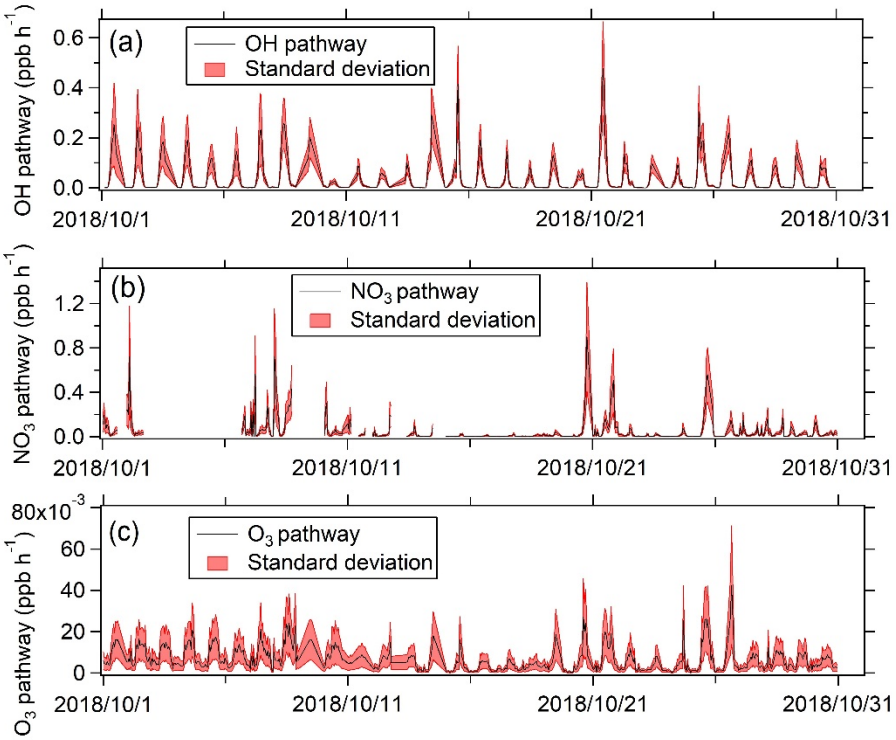

Figure S4. The uncertainty of gOON production rate of (a) OH, (b) NO_3 and (c) O_3 pathway by Monte Carlo method with 10,000 calculations. The shaded areas mean the standard deviations.

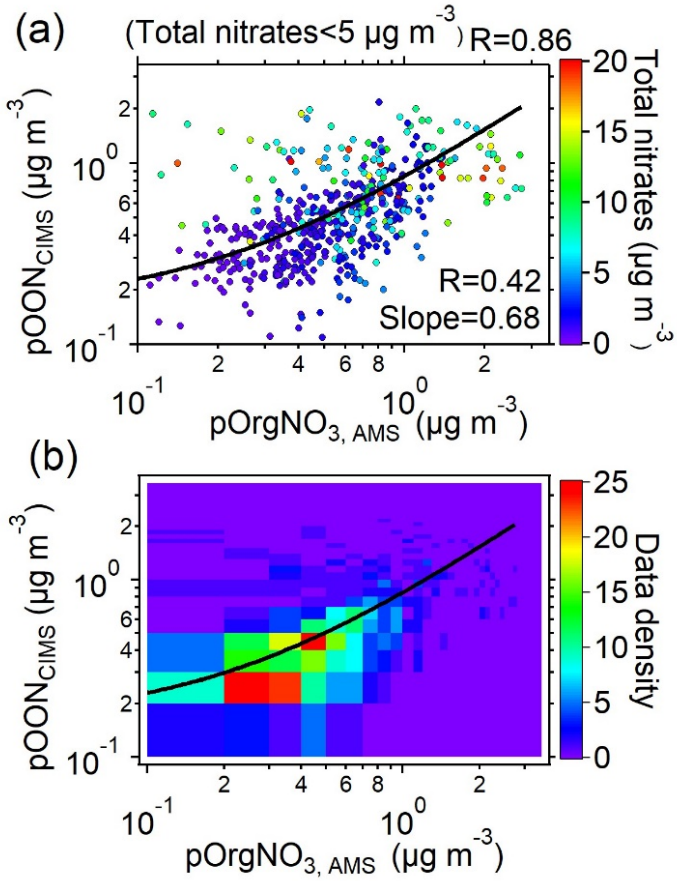

Figure S5. (a) Scatterplot of $pOON_{CIMS}$ versus $pOrgNO_{3,\ AMS}$ during the campaign. The points are color-coded using total nitrates (including inorganic nitrate and organic nitrate) measured by AMS. (b) The corresponding joint histogram which the pixels have a resolution of 0.1 μg m^{-3} and color-coded using data density.

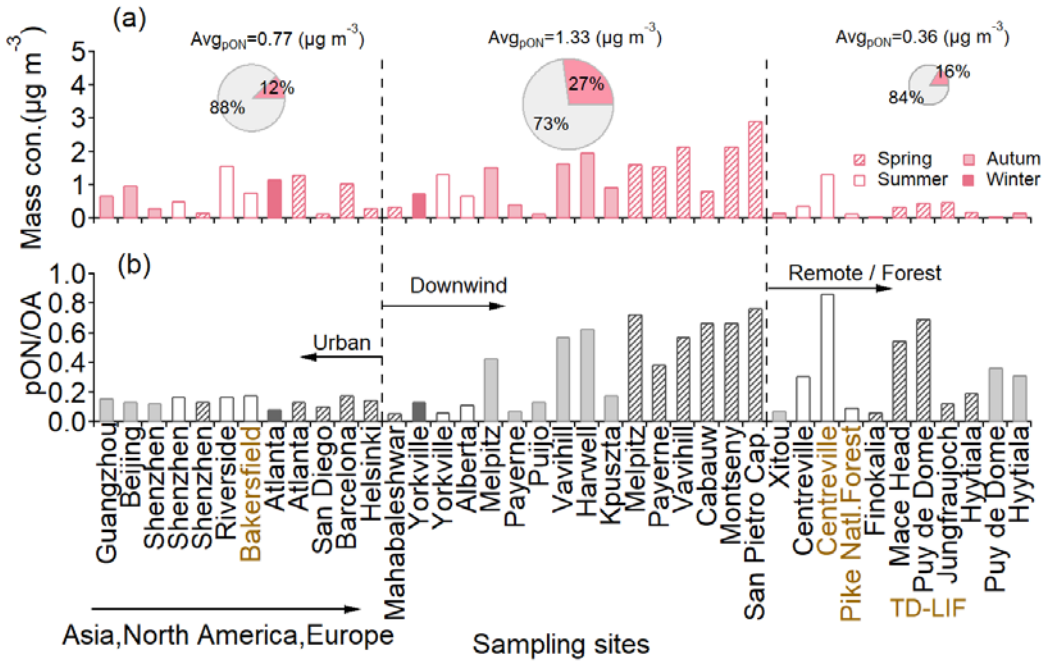

Figure S6. (a) Mass concentration pON and (b) its fraction to OA at sites around the world (Ayres et al., 2015; Day et al., 2010; Farmer et al., 2010; Fisher et al., 2016; Fry et al., 2013; Kiendler-Scharr et al., 2016; Lanz et al., 2010; Lee et al., 2019; Rollins et al., 2012; Salvador et al., 2020; Singla et al., 2019; Xu et al., 2015; Yu et al., 2019) classified into urban sites, downwind sites (lied downwind of the cities where were influenced by the emissions from the cities), forest or remote sites with different seasons. The average molecular weight of ON used for all sites is assumed to be 200 g mol^{-1}. The inset pies indicate the average fraction of pON (pink) to OA at each type of site. The yellow indicates the data are measured by thermal dissociation laser-induced fluorescence instrument (TD-LIF). The method of the pON$_{AMS/TD-LIF}$/OA calculation was referred to Takeuchi and Ng (2019).

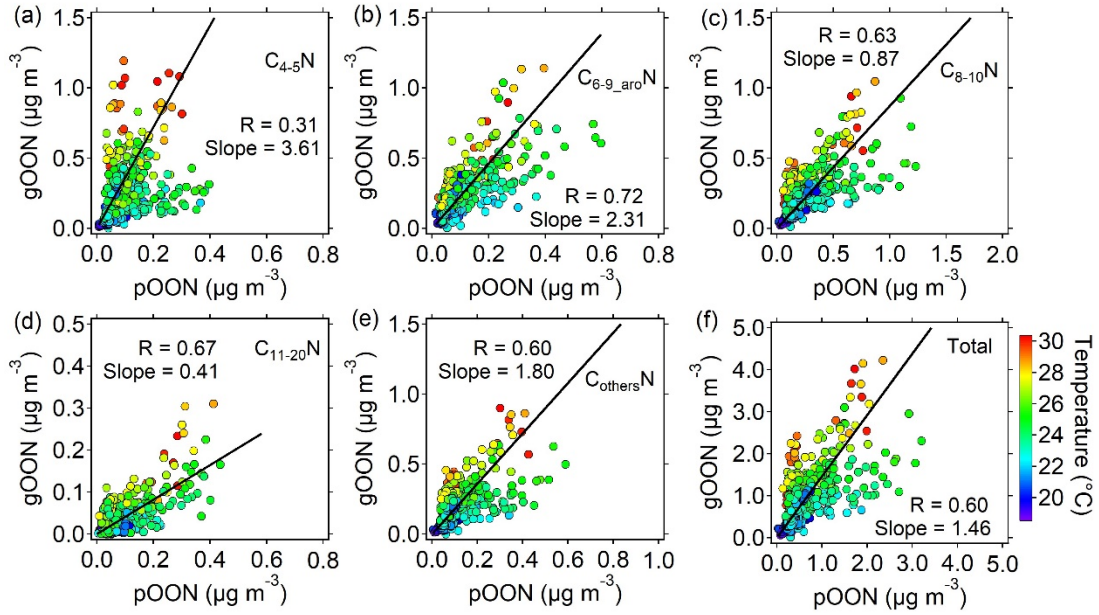

Figure S7. Scatter plots between gOON and pOON in different categories, i.e., (a) $C_{4-5}N$, (b) $C_{6-9\_aro}N$, (c) $C_{8-10}N$, (d) $C_{11-20}N$, (e) $C_{other}N$ and (f) the total values. The plots are color-coded by ambient temperature.

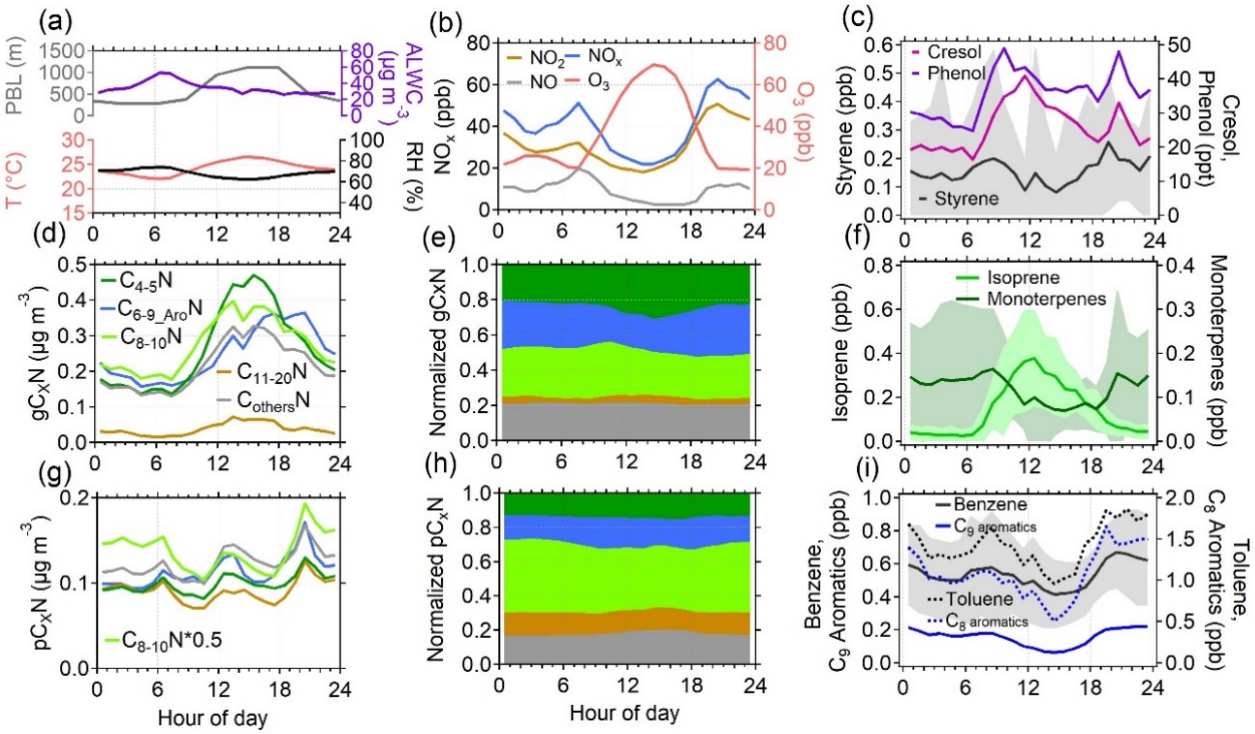

Figure S8. The average diurnal variations of (a) planetary boundary layer height (PBL), aerosol liquid water contents (ALWC), temperature (T) and relative humidity (RH), (b) mixing ratios of nitrogen dioxide (NO_2), nitric oxide (NO), NO_x (NO_x = NO + NO_2), and ozone (O_3), (c) cresol, phenol, and styrene, (d) gas phase, and (g) particle phase C_xN groups measured by the CIMS, mass fraction of (e) gas- and (h) particle-phase C_xN groups, (f) isoprene and monoterpenes, (i) benzene, toluene, C_8 aromatics, C_9 aromatics during the campaign of October. The shaded areas mean the standard deviations.

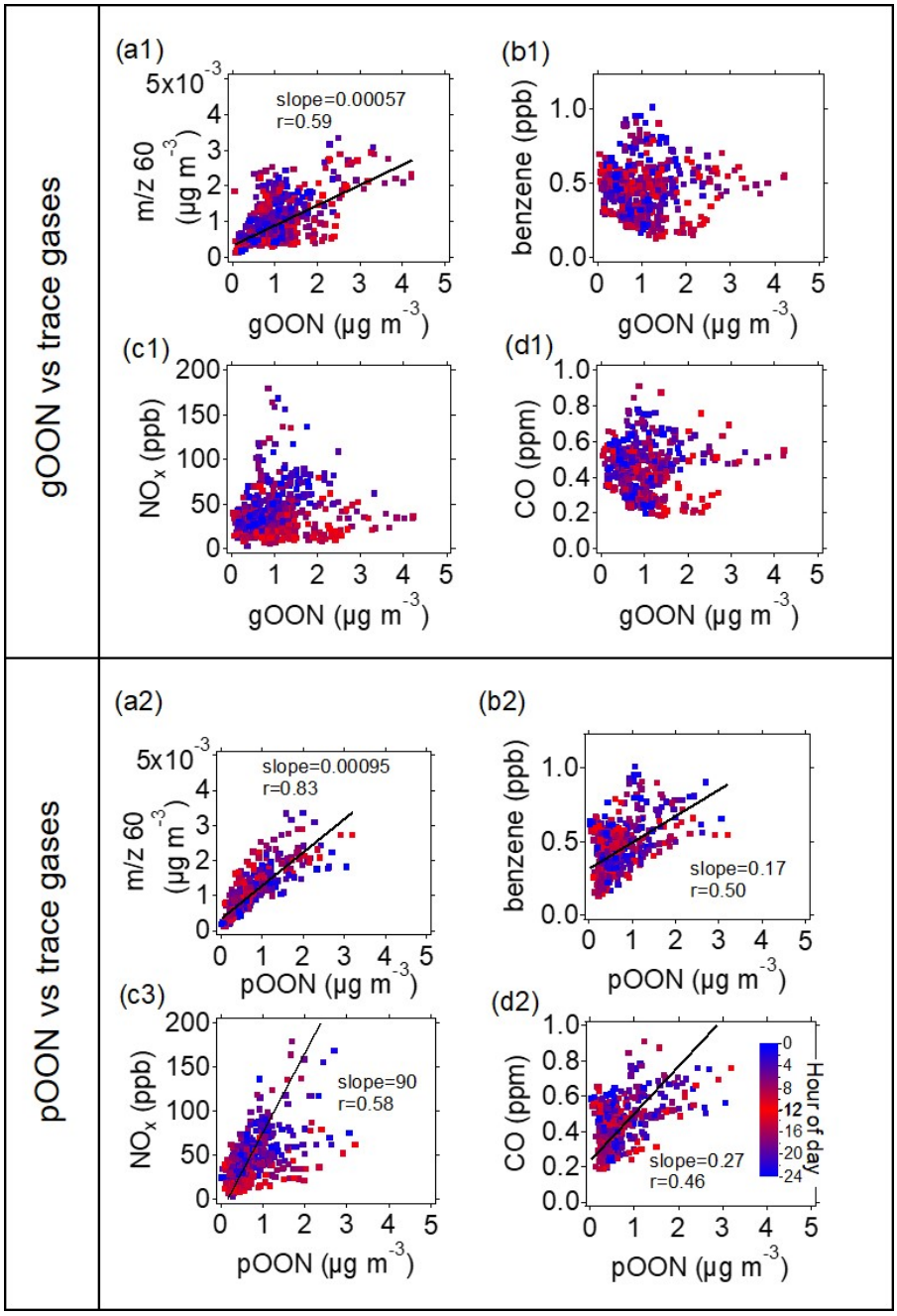

Figure S9. Scatter plots between gOON (up panel) or pOON (down panel) measured by the CIMS and (a1, a2) *m/z* 60 fragment, (b1, b2) benzene, (c1, c2) NO_x, (d1, d2) carbon monoxide (CO). All scatter plots are color-coded using hour of the day. The HR peak, $C_2H_4O_2^+$, representing the levoglucosan, show similar variation as *m/z* 60.

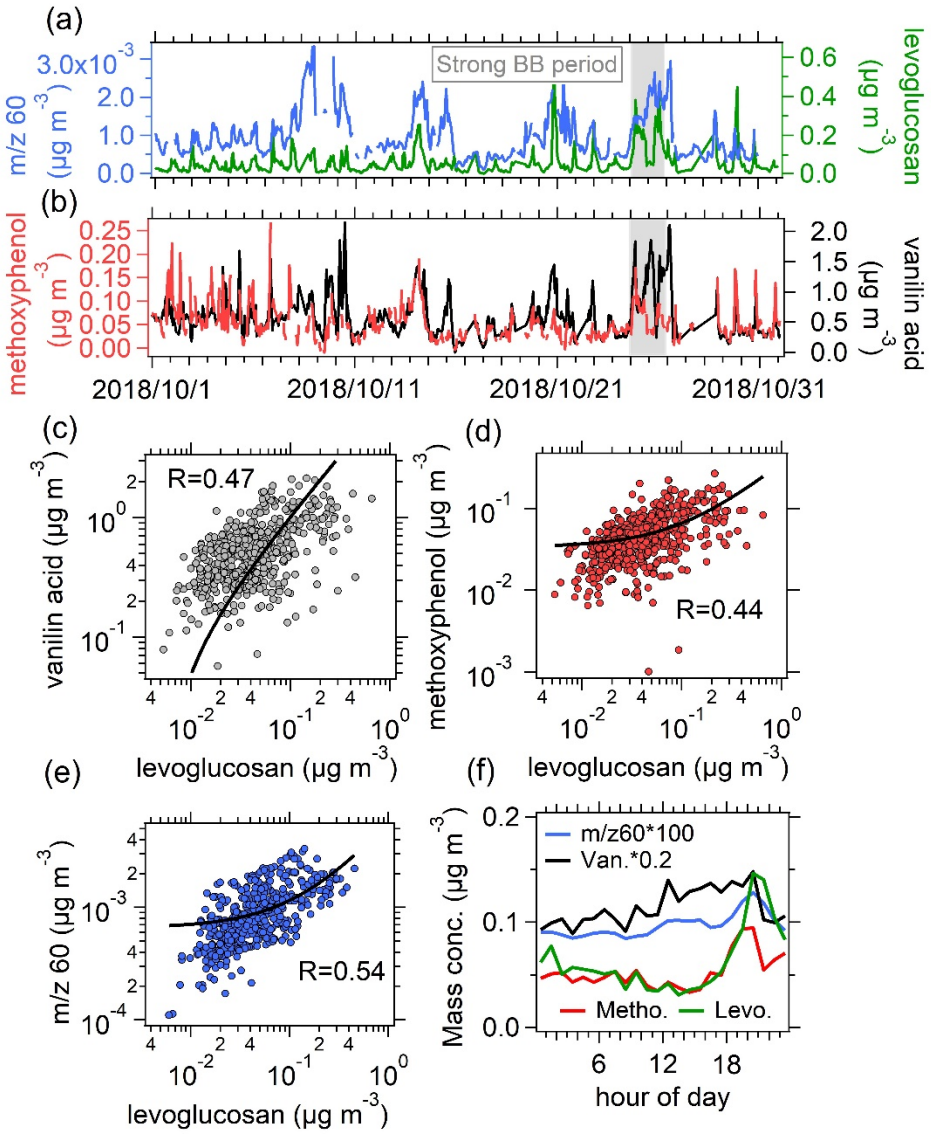

Figure S10. (a) Time series of *m/z* 60 from the AMS, particulate levoglucosan ($C_6H_{10}O_5I^-$), (b) methoxyphenol and vanillin acid from CIMS. The *m/z* 60 was found to be a fragment from levoglucosan-like species and supposed to be a tracer of biomass burning (Cubison et al., 2011). Scatter plots of (c) methoxyphenol, (d) vanillin acid, and (e) *m/z* 60 versus levoglucosan. Moderate agreement between them and levoglucosan also demonstrates the existence of biomass burning emissions (Urban et al., 2012). (f) Diurnal variation of the four species.

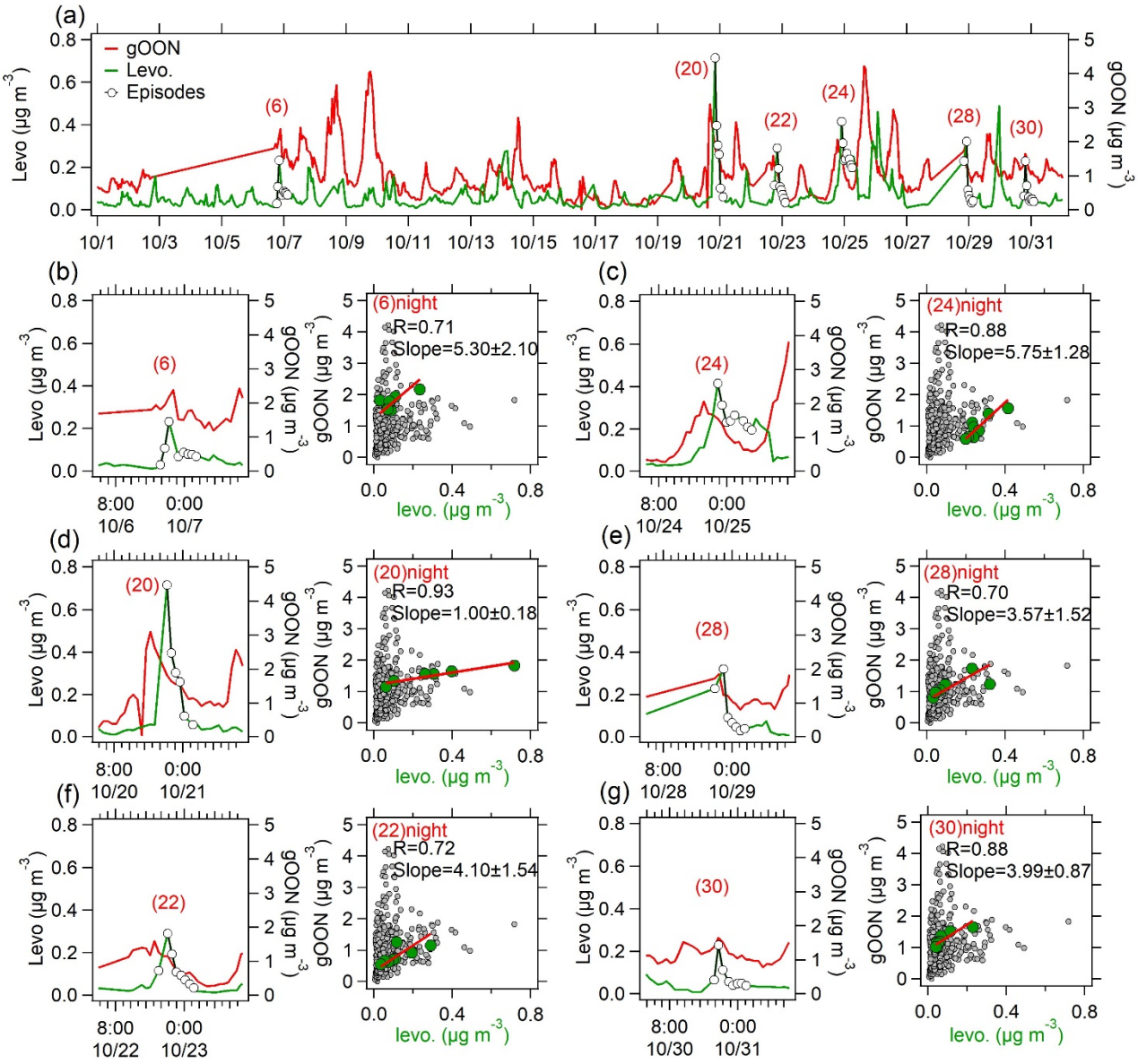

Figure S11. (a) Time series of measured gOON and levoglucosan (levo.) measured by the CIMS. The biomass burning episodes are labeled based on selection criteria as well. (b–f) Six episodes were selected and used for calculating biomass burning ratios between gOON and levoglucosan. The time series and scatter plots during each episode are also shown here.

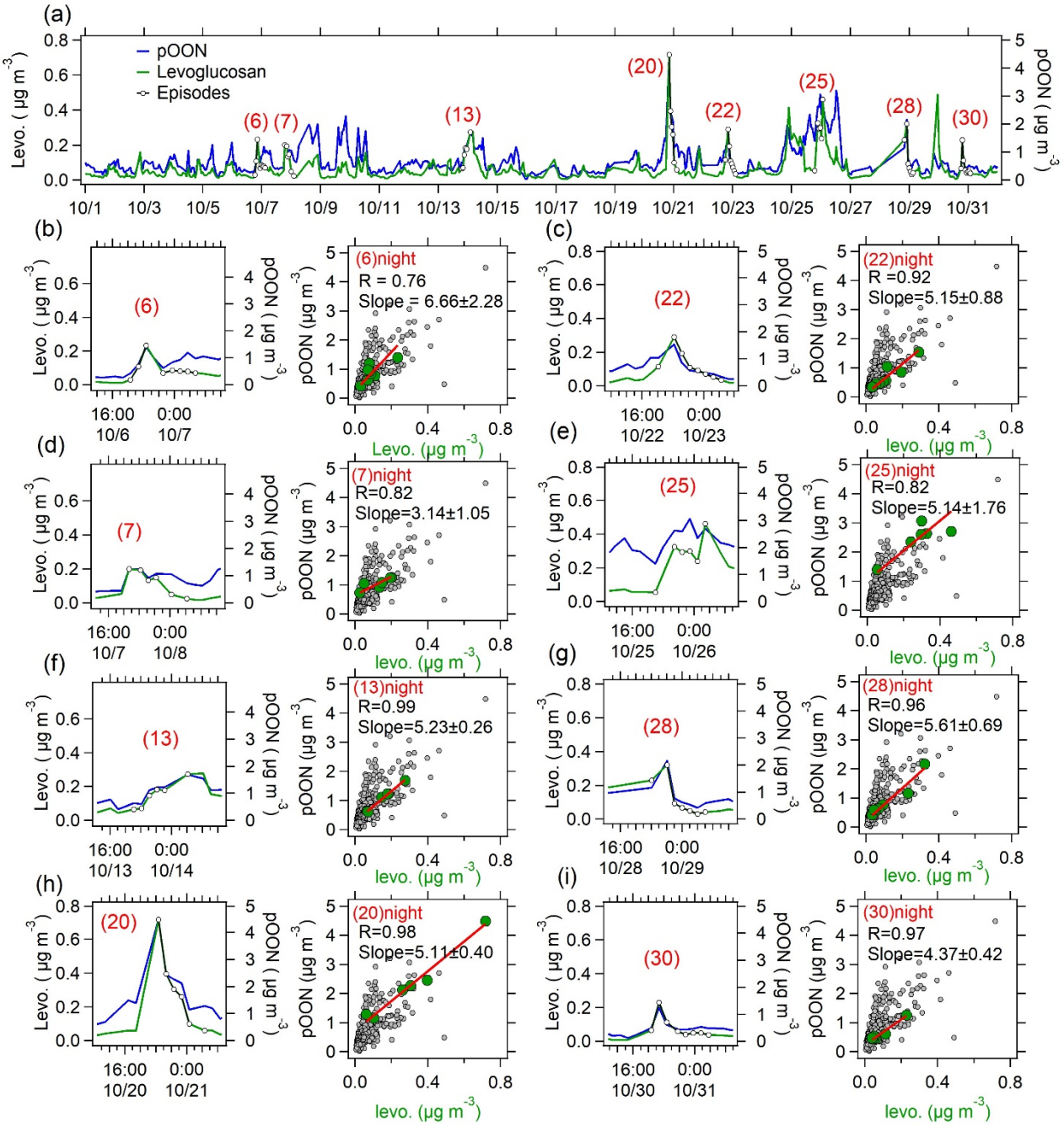

Figure S12. (a) Time series of pOON and levoglucosan (levo.) measured by the CIMS. The biomass burning episodes are labeled based on the selection criteria as well. (b−i) Eight episodes were selected and used for calculating biomass burning ratios between pOON and levoglucosan. The time series and scatter plots during each episode are shown here.

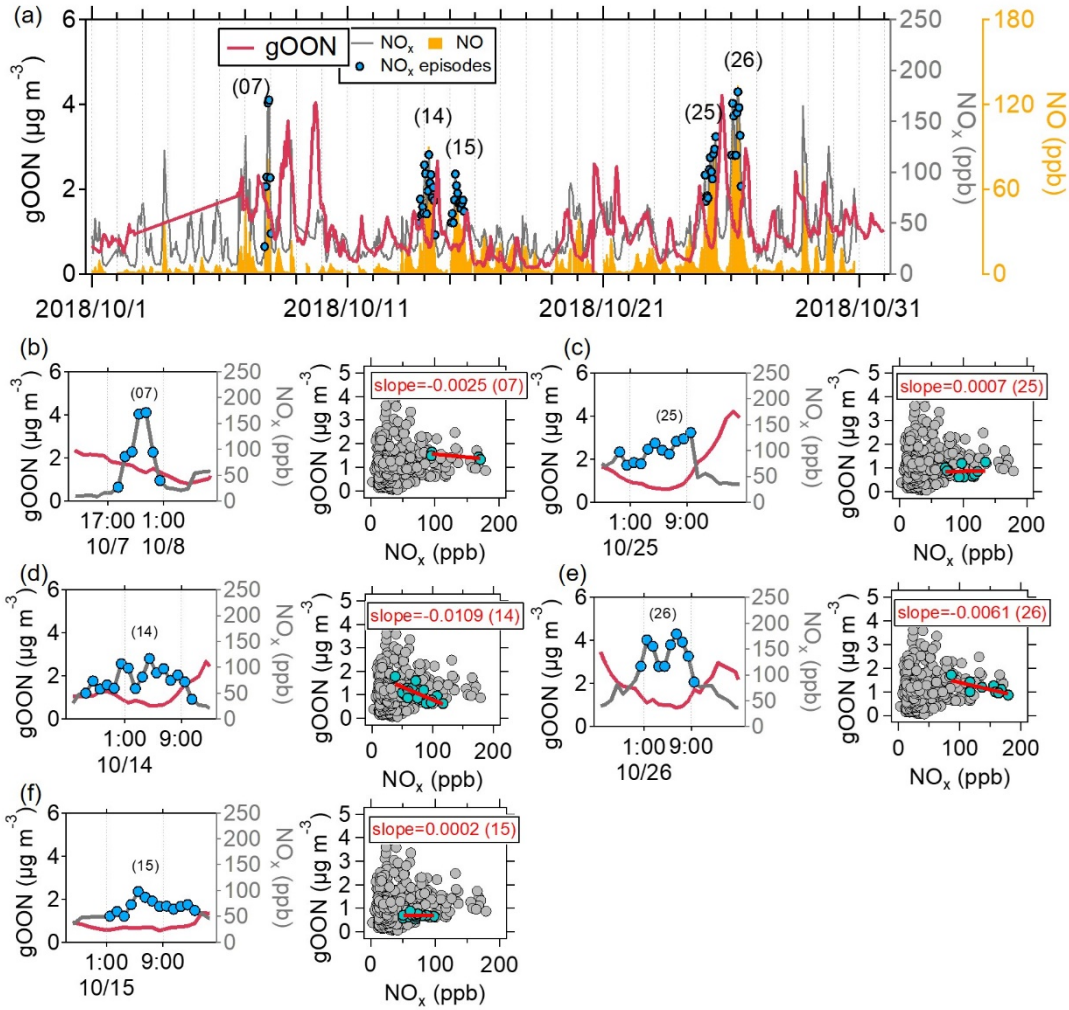

Figure S13. (a) Time series of gOON measured by the CIMS, and NO/NO_x measured by a NO_x analyzer. The episodes are labeled based on the high concentration of NO_x. (b−f) Time series and scatter plots of gOON vs NO_x during five selected NO_x polluted episodes. NO_x was the tracer for vehicle emissions (Harrison et al., 2003; Krecl et al., 2017). The extremely high NO concentrations (100−200 ppb) indicate strong influences from fresh vehicle emissions. No consistent enhancement between gOON and NO_x was found during the high NO_x episodes, suggesting the vehicle emission is not an important source of gOON in the ambient air.

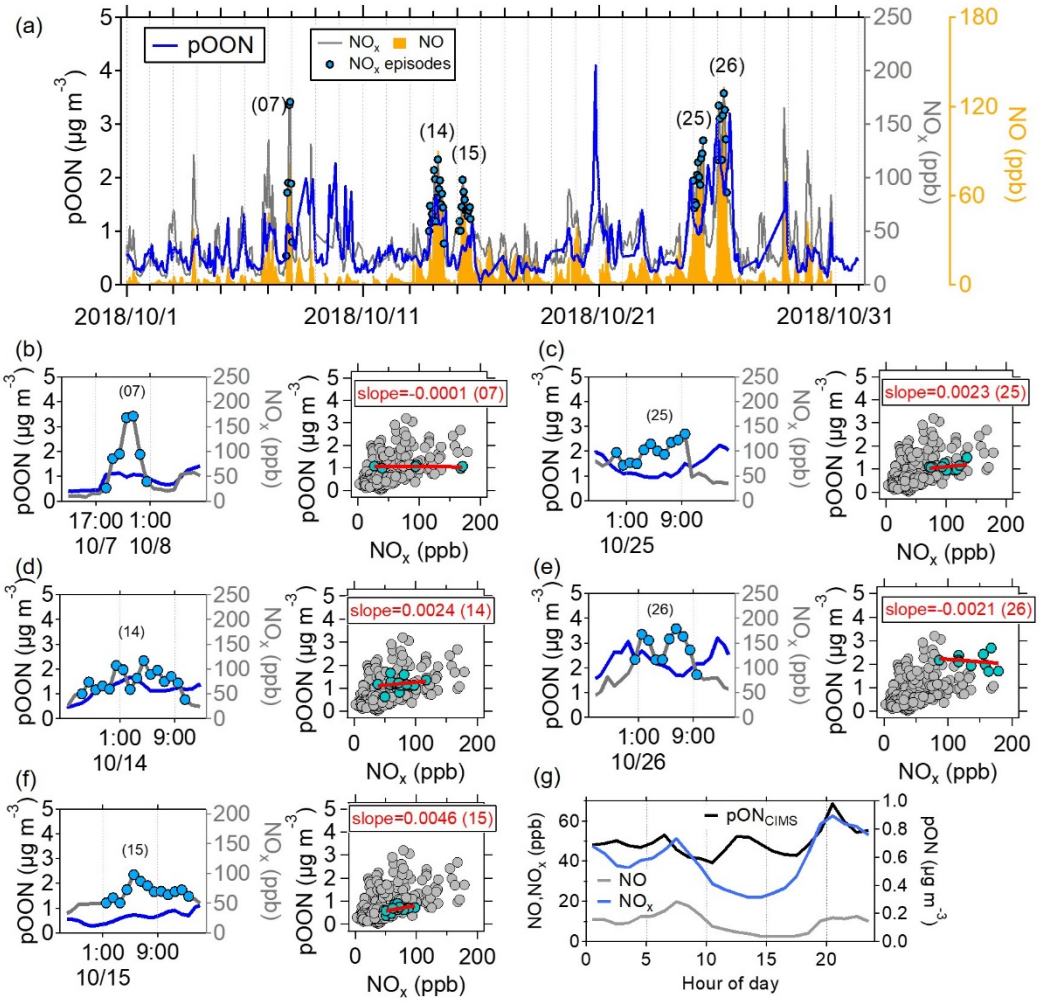

Figure S14. (a) Time series of pOON measured by the CIMS, and NO/NO_x measured by the NO_x analyzer. The episodes are labeled based on the high concentration of NO_x. (b−f) Time series and scatter plots of pOON vs NO_x during five selected NO_x polluted episodes. (g) Diurnal variations of the measured pOON by the CIMS ($pOON_{CIMS}$), NO and NO_x. NO_x was the tracer for vehicle emissions (Harrison et al., 2003; Krecl et al., 2017). The extremely high NO concentrations (100−200 ppb) indicate strong influence from fresh vehicle emissions during that episode. However, no consistent enhancement between pOON and NO_x was found during these high NO_x episodes, suggesting the vehicle emission is not an important source of pOON in this study.

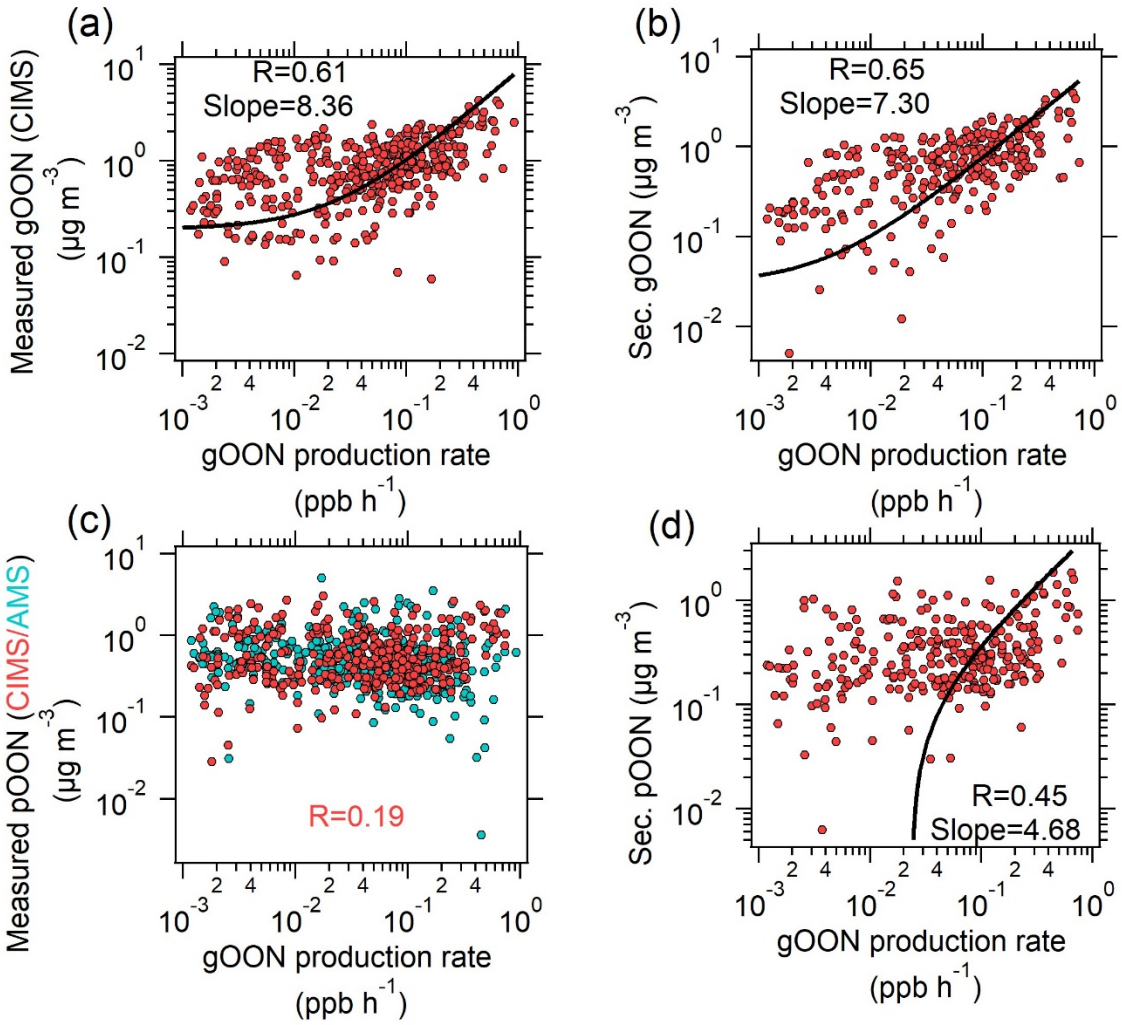

Figure S15. Scatter plots between (a) measured gOON and (b) secondary gOON vs total secondary gOON production rate. Scatter plots of (c) measured pOON and (d) secondary pOON vs total secondary gOON production rate. The logarithm is applied for both axes.

Figure S16. The field points of active fires or thermal anomalies from Modis Satellite around the sampling site, Guangzhou Institute of Geochemistry (GIG), in Guangzhou during the strong biomass burning period October 24−26th. (Source: from the Fire Information for Resource Management System (FIRMS), https://firms.modaps.eosdis. nasa.gov).

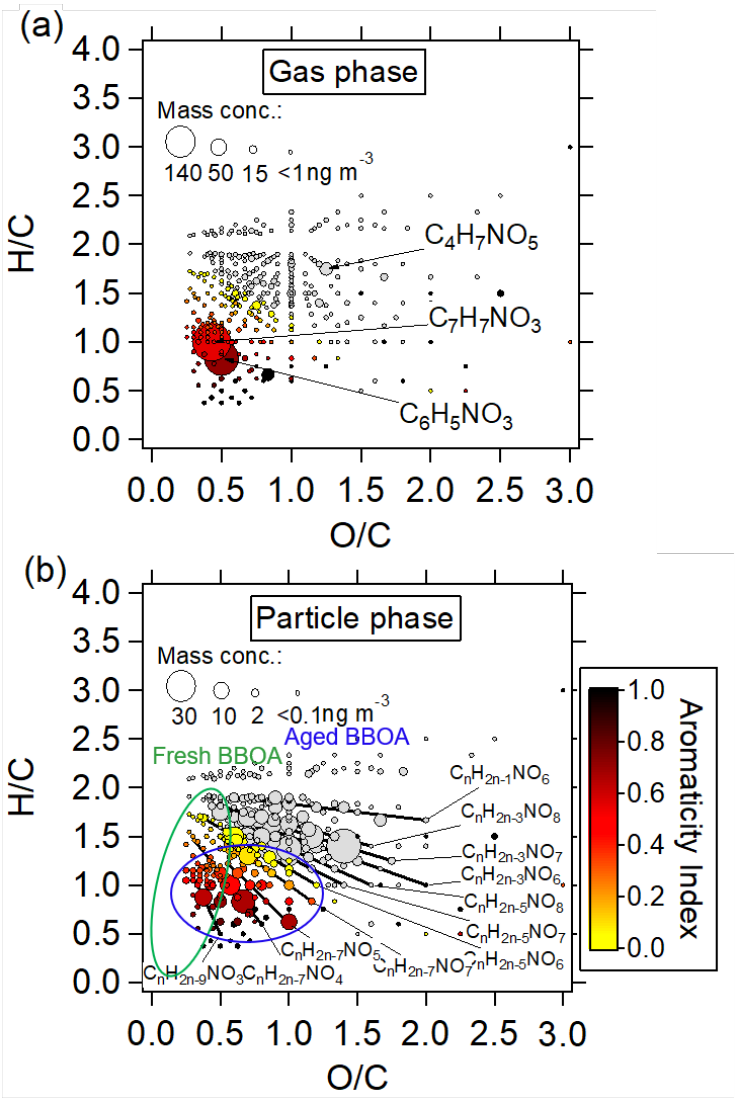

Figure S17. Van Krevelen (VK) diagram of all compounds from (a) gOON and (b) pOON. The size of symbols is proportional to the mean enhanced concentrations at 20:00 on October 22 of each compound. Ions are color-coded with Aromaticity Index between 0 and 1 (Wang et al., 2019). The green and blue ellipse represent OA from freshly emitted and aged biomass burning plumes, respectively, based on orbitrap (ESI^-) measurement in Wang et al. (2019). During the whole campaign, the most contributive species are $C_4H_7NO_5$ (7.9%), $C_6H_5NO_3$ (7.4%) and $C_7H_7NO_3$ (5.9%) in the gas phase and $C_8H_{11}NO_7$ (7.9%) in the particle phase. The enhancement concentration of $C_4H_7NO_5$ is much lower than its mean value, implying secondary formation is its dominant source.

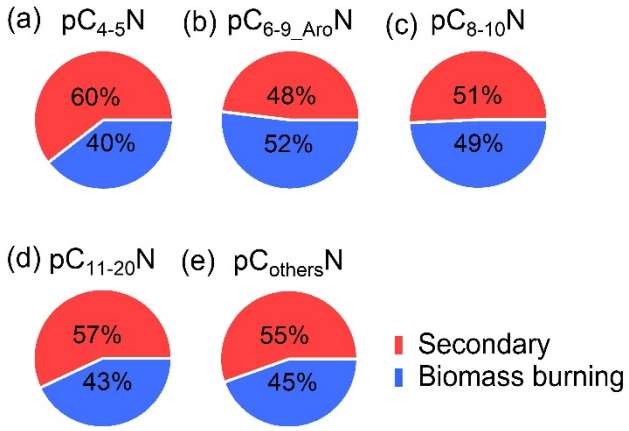

Figure S18. The contributions of biomass burning and secondary formation to each particle-phase C_xN (pC_xN) group following Eqs. (1) and (2) in section 3.2.

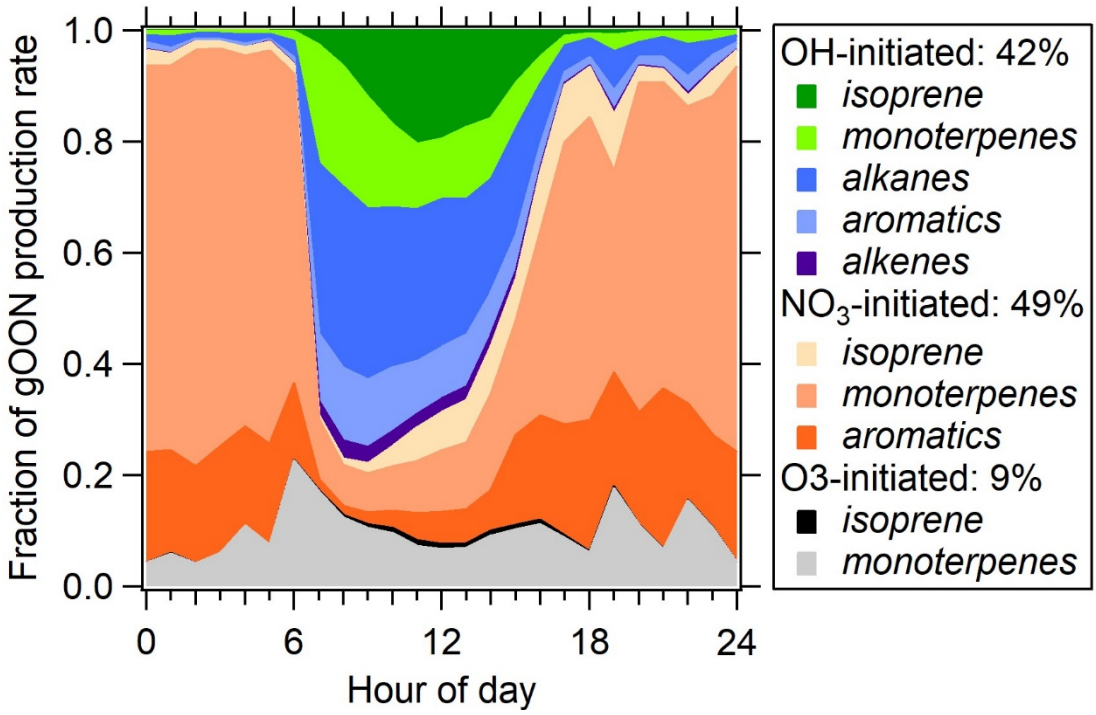

Figure S19. Average diurnal variations of the fractions of gOON production rate from OH initiated, NO_3 initiated and O_3 initiated oxidation pathways. For each pathway, contributions from classified VOCs are also shown.

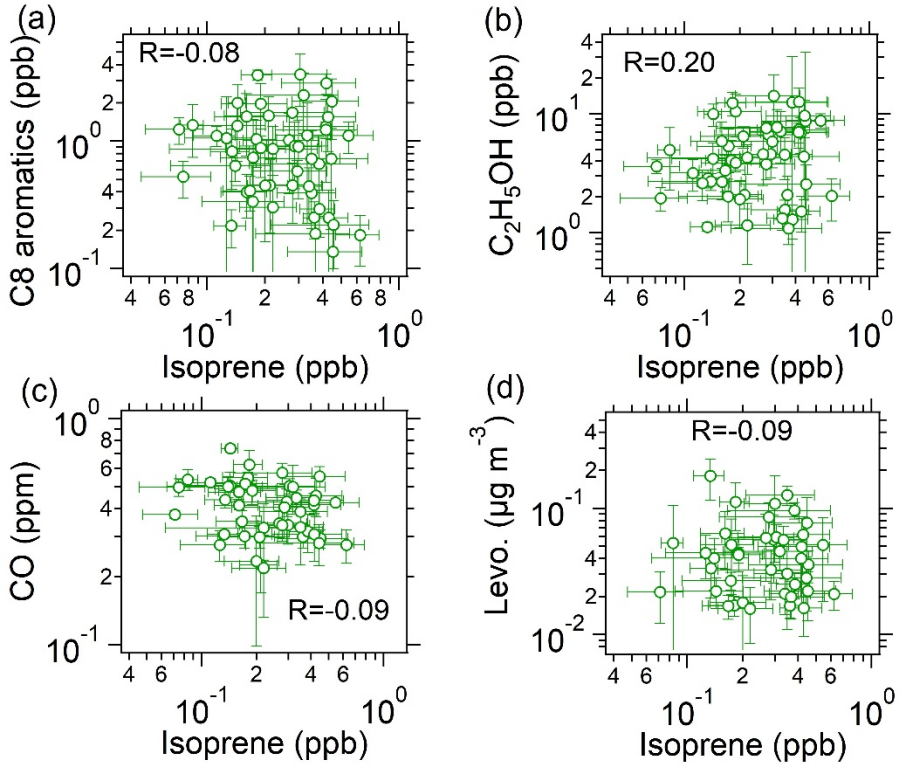

Figure S20. Scatter plots between the averaged (a) C8 aromatics, (b) ethanol, (c) CO, and (d) levoglucosan vs isoprene during daytime (9:00−18:00) during the entire campaign. The error bars are standard deviations of average values during daytime. The logarithm is applied for both axes.

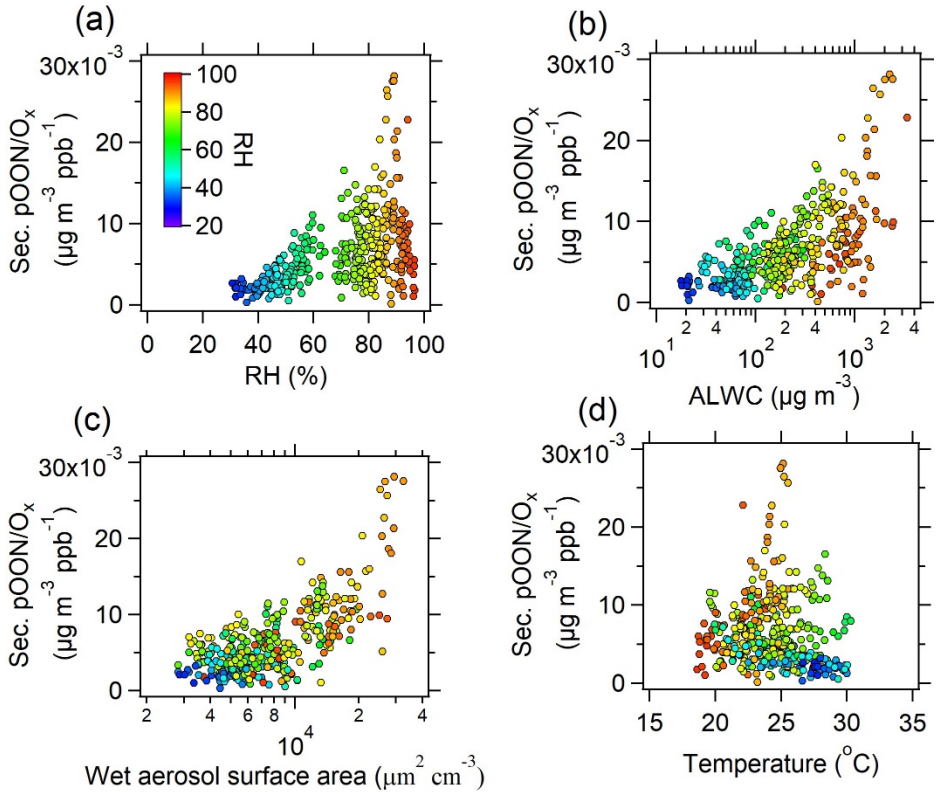

Figure S21. The ratio of Secondary (Sec.) pOON to O_x versus the (a) RH, (b) aerosol liquid water content (ALWC), (c) wet aerosol surface area, and (d) ambient temperature color-coded using the RH during the campaign.

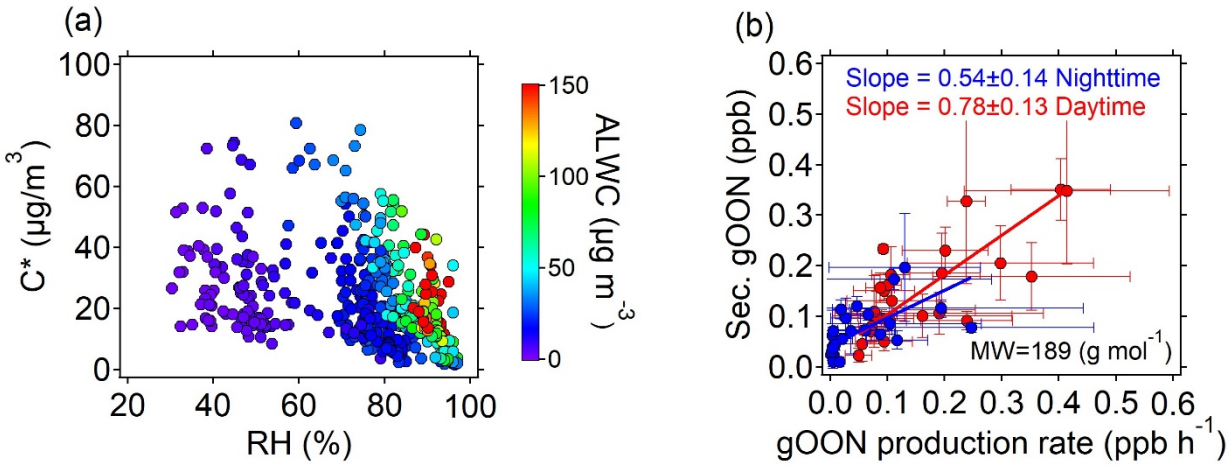

Figure S22. (a) Scatterplot of saturation mass concentration of total OON (C^* = 1/(C_p/C_{OA}/C_g)) versus RH color-coded with ALWC. (b) Scatter plot between secondary gOON concentration and gOON production rate. The regression slope can be used to estimate the lifetime of gOON following Liebmann et al. (2019).

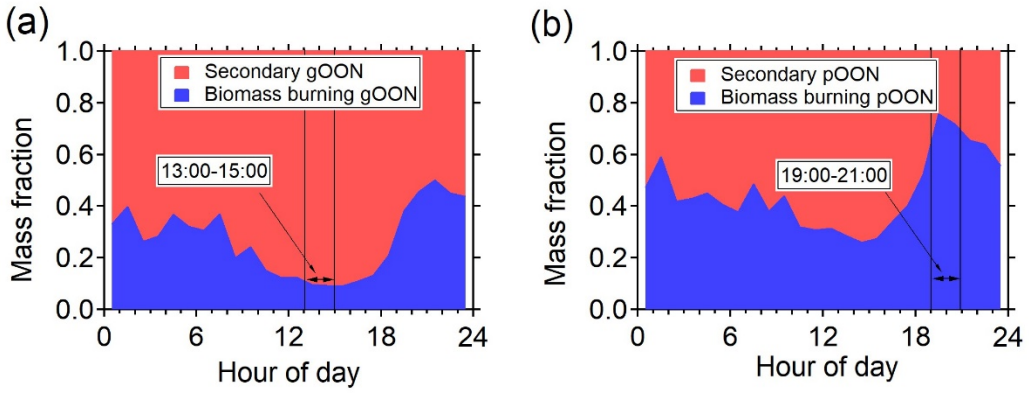

Figure S23. The average diurnal mass fractions of the contributions from secondary formation and biomass burning to (a) gOON and (b) pOON, respectively. The time periods of 13:00−15:00 and 19:00−21:00 represented the secondary formation dominated period and biomass burning dominated period for the particle phase, respectively.

Reference

Ayres, B. R., Allen, H. M., Draper, D. C., Brown, S. S., Wild, R. J., Jimenez, J. L., Day, D. A., Campuzano-Jost, P., Hu, W., de Gouw, J., Koss, A., Cohen, R. C., Duffey, K. C., Romer, P., Baumann, K., Edgerton, E., Takahama, S., Thornton, J. A., Lee, B. H., Lopez-Hilfiker, F. D., Mohr, C., Wennberg, P. O., Nguyen, T. B., Teng, A., Goldstein, A. H., Olson, K., and Fry, J. L.: Organic nitrate aerosol formation via NO3+ biogenic volatile organic compounds in the southeastern United States, Atmos. Chem. Phys., 15, 13377-13392, https://doi.org/10.5194/acp-15-13377-2015, 2015.

Boyd, C. M., Sanchez, J., Xu, L., Eugene, A. J., Nah, T., Tuet, W. Y., Guzman, M. I., and Ng, N. L.: Secondary organic aerosol formation from the β-pinene+NO3 system: effect of humidity and peroxy radical fate, Atmos. Chem. Phys., 15, 7497-7522, https://doi.org/10.5194/acp-15-7497-2015, 2015.

Brown, S. S. and Stutz, J.: Nighttime radical observations and chemistry, Chem Soc Rev, 41, 6405-6447, 10.1039/c2cs35181a, 2012.

Cubison, M. J., Ortega, A. M., Hayes, P. L., Farmer, D. K., Day, D., Lechner, M. J., Brune, W. H., Apel, E., Diskin, G. S., Fisher, J. A., Fuelberg, H. E., Hecobian, A., Knapp, D. J., Mikoviny, T., Riemer, D., Sachse, G. W., Sessions, W., Weber, R. J., Weinheimer, A. J., Wisthaler, A., and Jimenez, J. L.: Effects of aging on organic aerosol from open biomass burning smoke in aircraft and laboratory studies, Atmos. Chem. Phys., 11, 12049-12064, https://doi.org/10.5194/acp-11-12049-2011, 2011.

Dancey, C. and Reidy, J.: Statistics without Maths for Psychology, London: Prentice Hall Paerson.2007.

Day, D. A., Liu, S., Russell, L. M., and Ziemann, P. J.: Organonitrate group concentrations in submicron particles with high nitrate and organic fractions in coastal southern California, Atmos. Environ., 44, 1970-1979, 10.1016/j.atmosenv.2010.02.045, 2010.

Day, D. A., Campuzano-Jost, P., Nault, B. A., Palm, B. B., Hu, W., Guo, H., Wooldridge, P. J., Cohen, R. C., Docherty, K. S., Huffman, J. A., de Sá, S. S., Martin, S. T., and Jimenez, J. L.: A systematic re-evaluation of methods for quantification of bulk particle-phase organic nitrates using real-time aerosol mass spectrometry, Atmos. Meas. Tech., 15, 459-483, 10.5194/amt-15-459-2022, 2022.

Farmer, D. K., Matsunaga, A., Docherty, K. S., Surratt, J. D., Seinfeld, J. H., Ziemann, P. J., and Jimenez, J. L.: Response of an aerosol mass spectrometer to organonitrates and organosulfates and implications for atmospheric chemistry, Proc. Natl. Acad. Sci. U. S. A., 107, 6670-6675, 10.1073/pnas.0912340107, 2010.

Fisher, J. A., Jacob, D. J., Travis, K. R., Kim, P. S., Marais, E. A., Miller, C. C., Yu, K., Zhu, L., Yantosca, R. M., Sulprizio, M. P., Mao, J., Wennberg, P. O., Crounse, J. D., Teng, A. P., Nguyen, T. B., St Clair, J. M., Cohen, R. C., Romer, P., Nault, B. A., Wooldridge, P. J., Jimenez, J. L., Campuzano-Jost, P., Day, D. A., Hu, W., Shepson, P. B., Xiong, F., Blake, D. R., Goldstein, A. H., Misztal, P. K., Hanisco, T. F., Wolfe, G. M., Ryerson, T. B., Wisthaler, A., and Mikoviny, T.: Organic nitrate chemistry and its implications for nitrogen budgets in an isoprene- and monoterpene-rich atmosphere: constraints from

aircraft (SEAC(4)RS) and ground-based (SOAS) observations in the Southeast US, Atmos. Chem. Phys., 16, 5969-5991, 10.5194/acp-16-5969-2016, 2016.

Fry, J. L., Draper, D. C., Zarzana, K. J., Campuzano-Jost, P., Day, D. A., Jimenez, J. L., Brown, S. S., Cohen, R. C., Kaser, L., Hansel, A., Cappellin, L., Karl, T., Roux, A. H., Turnipseed, A., Cantrell, C., Lefer, B. L., and Grossberg, N.: Observations of gas- and aerosol-phase organic nitrates at BEACHON-RoMBAS 2011, Atmos. Chem. Phys., 13, 8585-8605, 10.5194/acp-13-8585-2013, 2013.

Fry, J. L., Brown, S. S., Middlebrook, A. M., Edwards, P. M., Campuzano-Jost, P., Day, D. A., Jimenez, J. L., Allen, H. M., Ryerson, T. B., Pollack, I., Graus, M., Warneke, C., de Gouw, J. A., Brock, C. A., Gilman, J., Lerner, B. M., Dubé, W. P., Liao, J., and Welti, A.: Secondary organic aerosol (SOA) yields from NO3 radical + isoprene based on nighttime aircraft power plant plume transects, Atmos. Chem. Phys., 18, 11663-11682, 10.5194/acp-18-11663-2018, 2018.

Gkatzelis, G. I., Coggon, M. M., McDonald, B. C., Peischl, J., Aikin, K. C., Gilman, J. B., Trainer, M., and Warneke, C.: Identifying Volatile Chemical Product Tracer Compounds in U.S. Cities, Environ. Sci. Technol., 55, 188-199, https://doi.org/10.1021/acs.est.0c05467, 2021.

Hamilton, J. F., Bryant, D. J., Edwards, P. M., Ouyang, B., Bannan, T. J., Mehra, A., Mayhew, A. W., Hopkins, J. R., Dunmore, R. E., Squires, F. A., Lee, J. D., Newland, M. J., Worrall, S. D., Bacak, A., Coe, H., Percival, C., Whalley, L. K., Heard, D. E., Slater, E. J., Jones, R. L., Cui, T., Surratt, J. D., Reeves, C. E., Mills, G. P., Grimmond, S., Sun, Y., Xu, W., Shi, Z., and Rickard, A. R.: Key Role of NO3 Radicals in the Production of Isoprene Nitrates and Nitrooxyorganosulfates in Beijing, Environ. Sci. Technol., 55, 842-853, https://doi.org/10.1021/acs.est.0c05689, 2021.

Hao, L. Q., Kortelainen, A., Romakkaniemi, S., Portin, H., Jaatinen, A., Leskinen, A., Komppula, M., Miettinen, P., Sueper, D., Pajunoja, A., Smith, J. N., Lehtinen, K. E. J., Worsnop, D. R., Laaksonen, A., and Virtanen, A.: Atmospheric submicron aerosol composition and particulate organic nitrate formation in a boreal forestland–urban mixed region, Atmos. Chem. Phys., 14, 13483-13495, https://doi.org/10.5194/acp-14-13483-2014, 2014.

Harrison, R. M., Tilling, R., Callén Romero, M. a. S., Harrad, S., and Jarvis, K.: A study of trace metals and polycyclic aromatic hydrocarbons in the roadside environment, Atmos. Environ., 37, 2391-2402, https://doi.org/10.1016/S1352-2310(03)00122-5, 2003.

Hilas, C. S., Goudos, S. K., and Sahalos, J. N.: Seasonal decomposition and forecasting of telecommunication data: A comparative case study, Technological Forecasting and Social Change, 73, 495-509, https://doi.org/10.1016/j.techfore.2005.07.002, 2006.

Huffman, J. A., Ziemann, P. J., Jayne, J. T., Worsnop, D. R., and Jimenez, J. L.: Development and Characterization of a Fast-Stepping/Scanning Thermodenuder for Chemically-Resolved Aerosol Volatility Measurements, Aerosol Sci. Technol., 42, 395-407, https://doi.org/10.1080/02786820802104981, 2008.

Kiendler-Scharr, A., Mensah, A. A., Friese, E., Topping, D., Nemitz, E., Prevot, A. S. H., Äijälä, M., Allan, J., Canonaco, F., Canagaratna, M., Carbone, S., Crippa, M., Dall Osto, M., Day, D. A., De Carlo, P., Di Marco, C. F., Elbern, H., Eriksson, A., Freney, E., Hao, L., Herrmann, H., Hildebrandt, L., Hillamo, R., Jimenez, J. L., Laaksonen, A., McFiggans, G., Mohr, C., O'Dowd, C., Otjes, R., Ovadnevaite, J., Pandis, S. N., Poulain, L., Schlag, P., Sellegri, K., Swietlicki, E., Tiitta, P., Vermeulen, A., Wahner, A., Worsnop, D., and Wu, H. C.: Ubiquity of organic nitrates from nighttime chemistry in the European submicron aerosol, Geophys. Res. Lett., 43, 7735-7744, https://doi.org/10.1002/2016gl069239, 2016.

Koch, B. P. and Dittmar, T.: From mass to structure: an aromaticity index for high-resolution mass data of natural organic matter, Rapid Commun. Mass Spectrom., 20, 926-932, https://doi.org/10.1002/rcm.2386, 2006.

Koch, B. P. and Dittmar, T.: From mass to structure: an aromaticity index for high-resolution mass data of natural organic matter, Rapid Commun. Mass Spectrom., 30, 250-250, https://doi.org/10.1002/rcm.7433, 2016.

Krecl, P., Johansson, C., Targino, A. C., Ström, J., and Burman, L.: Trends in black carbon and size-resolved particle number concentrations and vehicle emission factors under real-world conditions, Atmos. Environ., 165, 155-168, https://doi.org/10.1016/j.atmosenv.2017.06.036, 2017.

Lanz, V. A., Prévôt, A. S. H., Alfarra, M. R., Weimer, S., Mohr, C., DeCarlo, P. F., Gianini, M. F. D., Hueglin, C., Schneider, J., Favez, O., D'Anna, B., George, C., and Baltensperger, U.: Characterization of aerosol chemical composition with aerosol mass spectrometry in Central Europe: an overview, Atmos. Chem. Phys., 10, 10453-10471, https://doi.org/10.5194/acp-10-10453-2010, 2010.

Lee, A. K. Y., Adam, M. G., Liggio, J., Li, S.-M., Li, K., Willis, M. D., Abbatt, J. P. D., Tokarek, T. W., Odame-Ankrah, C. A., Osthoff, H. D., Strawbridge, K., and Brook, J. R.: A large contribution of anthropogenic organo-nitrates to secondary organic aerosol in the Alberta oil sands, Atmos. Chem. Phys., 19, 12209-12219, https://doi.org/10.5194/acp-19-12209-2019, 2019.

Li, X. B., Yuan, B., Wang, S., Wang, C., Lan, J., Liu, Z., Song, Y., He, X., Huangfu, Y., Pei, C., Cheng, P., Yang, S., Qi, J., Wu, C., Huang, S., You, Y., Chang, M., Zheng, H., Yang, W., Wang, X., and Shao, M.: Variations and sources of volatile organic compounds (VOCs) in urban region: insights from measurements on a tall tower, Atmos. Chem. Phys., 22, 10567-10587, 10.5194/acp-22-10567-2022, 2022.

Liebmann, J., Sobanski, N., Schuladen, J., Karu, E., Hellén, H., Hakola, H., Zha, Q., Ehn, M., Riva, M., Heikkinen, L., Williams, J., Fischer, H., Lelieveld, J., and Crowley, J. N.: Alkyl nitrates in the boreal forest: formation via the NO3-, OH- and O3 induced oxidation of biogenic volatile organic compounds and ambient lifetimes, Atmos. Chem. Phys., 19, 10391-10403, https://doi.org/10.5194/acp-19-10391-2019, 2019.

McKay, M. D., Beckman, R. J., and Conover, W. J.: A Comparison of Three Methods for Selecting Values of Input Variables in the Analysis of Output From a Computer Code, Technometrics, 42, 55-61, 10.1080/00401706.2000.10485979, 2000.

Ng, N. L., Brown, S. S., Archibald, A. T., Atlas, E., Cohen, R. C., Crowley, J. N., Day, D. A., Donahue, N. M., Fry, J. L., Fuchs, H., Griffin, R. J., Guzman, M. I., Herrmann, H., Hodzic, A., Iinuma, Y., Jimenez, J. L., Kiendler-Scharr, A., Lee, B. H., Luecken, D. J., Mao, J., McLaren, R., Mutzel, A., Osthoff, H. D., Ouyang, B., Picquet-Varrault, B., Platt, U., Pye, H. O. T., Rudich, Y., Schwantes, R. H., Shiraiwa, M., Stutz, J., Thornton, J. A., Tilgner, A., Williams, B. J., and Zaveri, R. A.: Nitrate radicals and biogenic volatile organic compounds: oxidation, mechanisms, and organic aerosol, Atmos. Chem. Phys., 17, 2103-2162, https://doi.org/10.5194/acp-17-2103-2017, 2017.

Rollins, A. W., Browne, E. C., Min, K. E., Pusede, S. E., Wooldridge, P. J., Gentner, D. R., Goldstein, A. H., Liu, S., Day, D. A., Russell, L. M., and Cohen, R. C.: Evidence for NO(x) control over nighttime SOA formation, Science, 337, 1210-1212, https://doi.org/10.1126/science.1221520, 2012.

Salvador, C. M., Chou, C. C. K., Cheung, H. C., Ho, T. T., Tsai, C. Y., Tsao, T. M., Tsai, M. J., and Su, T. C.: Measurements of submicron organonitrate particles: Implications for the impacts of NOx pollution in a subtropical forest, Atmospheric Research, 245, https://doi.org/10.1016/j.atmosres.2020.105080, 2020.

Sato, K., Takami, A., Isozaki, T., Hikida, T., Shimono, A., and Imamura, T.: Mass spectrometric study of secondary organic aerosol formed from the photo-oxidation of aromatic hydrocarbons, Atmos. Environ., 44, 1080-1087, https://doi.org/10.1016/j.atmosenv.2009.12.013, 2010.

Singla, V., Mukherjee, S., Pandithurai, G., Dani, K. K., and Safai, P. D.: Evidence of Organonitrate Formation at a High Altitude Site, Mahabaleshwar, during the Pre-monsoon Season, Aerosol and Air Quality Research, 19, 1241-1251, https://doi.org/10.4209/aaqr.2018.03.0110, 2019.

Sommers, J. M., Stroud, C. A., Adam, M. G., O'Brien, J., Brook, J. R., Hayden, K., Lee, A. K. Y., Li, K., Liggio, J., Mihele, C., Mittermeier, R. L., Stevens, R. G., Wolde, M., Zuend, A., and Hayes, P. L.: Evaluating SOA formation from different sources of semi- and intermediate-volatility organic compounds from the Athabasca oil sands, Environmental Science: Atmospheres, 2, 469-490, 10.1039/D1EA00053E, 2022.

Sun, Y. L., Zhang, Q., Schwab, J. J., Yang, T., Ng, N. L., and Demerjian, K. L.: Factor analysis of combined organic and inorganic aerosol mass spectra from high resolution aerosol mass spectrometer measurements, Atmos. Chem. Phys., 12, 8537-8551, https://doi.org/10.5194/acp-12-8537-2012, 2012.

Takeuchi, M. and Ng, N. L.: Chemical composition and hydrolysis of organic nitrate aerosol formed from hydroxyl and nitrate radical oxidation of α-pinene and β-pinene, Atmos. Chem. Phys., 19, 12749-12766, https://doi.org/10.5194/acp-19-12749-2019, 2019.

Urban, R. C., Lima-Souza, M., Caetano-Silva, L., Queiroz, M. E. C., Nogueira, R. F. P., Allen, A. G., Cardoso, A. A., Held, G., and Campos, M. L. A. M.: Use of levoglucosan, potassium, and water-soluble organic carbon to characterize the origins of biomass-burning aerosols, Atmos. Environ., 61, 562-569, https://doi.org/10.1016/j.atmosenv.2012.07.082, 2012.

Wang, H., Lu, K., Chen, X., Zhu, Q., Chen, Q., Guo, S., Jiang, M., Li, X., Shang, D., Tan, Z., Wu, Y., Wu, Z., Zou, Q., Zheng, Y., Zeng, L., Zhu, T., Hu, M., and Zhang, Y.: High N2O5 Concentrations Observed in Urban Beijing: Implications of a Large

Nitrate Formation Pathway, Environmental Science & Technology Letters, 4, 416-420, https://doi.org/10.1021/acs.estlett.7b00341, 2017.

Wang, S., Peng, Y., Peng, Q., Wu, C., Wang, C., Wang, B., Wang, Z., Kuang, Y., Song, W., Wang, X., Hu, W., Chen, W., Shen, J., Chen, D., Shao, M., and Yuan, B.: Different chemical removal pathways of volatile organic compounds (VOCs): Comparison of urban and regional sites, Acta Sci. Circumstantiae, 40, 2311-2322, https://doi.org/10.13671/j.hjkxxb.2020.0153, 2020.

Wang, Y., Hu, M., Lin, P., Tan, T., Li, M., Xu, N., Zheng, J., Du, Z., Qin, Y., Wu, Y., Lu, S., Song, Y., Wu, Z., Guo, S., Zeng, L., Huang, X., and He, L.: Enhancement in Particulate Organic Nitrogen and Light Absorption of Humic-Like Substances over Tibetan Plateau Due to Long-Range Transported Biomass Burning Emissions, Environ. Sci. Technol., 53, 14222-14232, https://doi.org/10.1021/acs.est.9b06152, 2019.

Wolfe, G. M., Marvin, M. R., Roberts, S. J., Travis, K. R., and Liao, J.: The Framework for 0-D Atmospheric Modeling (F0AM) v3.1, Geosci. Model Dev., 9, 3309-3319, https://doi.org/10.5194/gmd-9-3309-2016, 2016.

Xu, L., Suresh, S., Guo, H., Weber, R. J., and Ng, N. L.: Aerosol characterization over the southeastern United States using high-resolution aerosol mass spectrometry: spatial and seasonal variation of aerosol composition and sources with a focus on organic nitrates, Atmos. Chem. Phys., 15, 7307-7336, https://doi.org/10.5194/acp-15-7307-2015, 2015.

Xu, W., Takeuchi, M., Chen, C., Qiu, Y., Xie, C., Xu, W., Ma, N., Worsnop, D. R., Ng, N. L., and Sun, Y.: Estimation of particulate organic nitrates from thermodenuder–aerosol mass spectrometer measurements in the North China Plain, Atmos. Meas. Tech., 14, 3693-3705, https://doi.org/10.5194/amt-14-3693-2021, 2021.

Yu, K., Zhu, Q., Du, K., and Huang, X.-F.: Characterization of nighttime formation of particulate organic nitrates based on high-resolution aerosol mass spectrometry in an urban atmosphere in China, Atmos. Chem. Phys., 19, 5235-5249, https://doi.org/10.5194/acp-19-5235-2019, 2019.

Zhu, Q., He, L. Y., Huang, X. F., Cao, L. M., Gong, Z. H., Wang, C., Zhuang, X., and Hu, M.: Atmospheric aerosol compositions and sources at two national background sites in northern and southern China, Atmos. Chem. Phys., 16, 10283-10297, 10.5194/acp-16-10283-2016, 2016.